Research Paper

High-efficient peroxymonosulfate activation for rapid atrazine degradation by FeSx@MoS2 derived from MIL-88A(Fe)

Fei Wang [a,b], Shan-Shan Liu [a,b], Ziyue Feng [a,b], Huifen Fu [a,b,*], Mengyu Wang [a,b], Peng Wang [a,b], Wen Liu [c], Chong-Chen Wang [a,b,*]

[a] Beijing Key Laboratory of Functional Materials for Building Structure and Environment Remediation, Beijing University of Civil Engineering and Architecture, Beijing 100044, PR China
[b] Beijing Energy Conservation & Sustainable Urban and Rural Development Provincial and Ministry Co-construction Collaboration Innovation Center, Beijing University of Civil Engineering and Architecture, Beijing 100044, PR China
[c] College of Environmental Sciences and Engineering, Peking University, The Key Laboratory of Water and Sediment Sciences, Ministry of Education, Beijing 100871, PR China

HIGHLIGHTS

- FeSx@MoS2-x heterojunction catalyst was synthesized adopting MIL-88A as precursor.
- The rapid regeneration of Fe^{2+} greatly promoted the SR-AOP performance.
- The continuous ATZ degradation was achieved via fixed bed reactor.

GRAPHICAL ABSTRACT
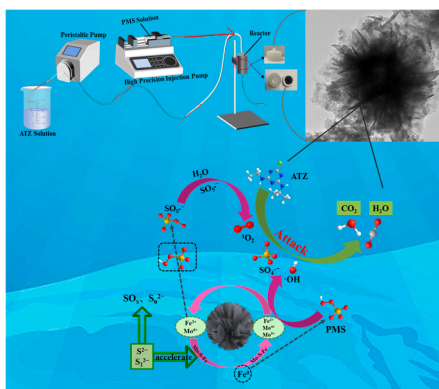
ARTICLE INFO

ABSTRACT

FeSx@MoS2-x (FM-x, x implied real Mo/Fe content ratios) in which FeSx derived from MIL-88A deposited on the surface of MoS2 with a tight heterogeneous interface were synthesized for peroxymonosulfate (PMS) activation to degrade atrazine (ATZ). The catalytic performance of FM-0.96 was greatly improved due to the rapid regeneration of Fe^{2+} resulting from the interfacial interaction. FM-0.96 could completely degrade 10.0 mg/L ATZ within 1.0 min, and the toxicities for most of its intermediates were greatly reduced. The k value of FM-0.96 was 320 and 40 times higher than that of the MoS_2 and FeS_x, respectively. The $SO_4{}^{\cdot-}$, $\cdot OH$ and $^1O_2$ were mainly responsible for ATZ degradation in FM-0.96/PMS system, and the conversion pathway of $^1O_2$ was analyzed. Furthermore, the long-term continuous operation for ATZ degradation was achieved using a fixed membrane

reactor. This work provides deep insights into metal sulfide composites derived from metal-organic frameworks for removing pollutants by activating PMS.

1. Introduction

Atrazine (ATZ), one of the most widely used herbicides in agriculture, is usually detected in the aquatic environment because of its long persistence, low biodegradability properties and so on, causing a threat to the aquatic environment (Li et al., 2019b). Moreover, it is reported that low ATZ dose can cause carcinogenesis, and its accumulations through the food chain have serious negative effects on humans (Zhang et al., 2018). Considering various conventional treatment methods cannot effectively remove ATZ from the aquatic environment, it is necessary to develop an effective method to remove ATZ.

Sulfate radical-based advanced oxidation processes (SR-AOPs) have been widely applied to the treatment of the organic contaminants in the aquatic environment due to their strong oxidation capacity (Duan et al., 2019; He et al., 2022; Zhang et al., 2022). In general, peroxymonosulfate (PMS) can be effectively activated by heat, UV light, ultrasound and transition metal catalysts to produce reactive oxygen species (ROS) (Yang et al., 2022; Yu et al., 2022). Especially, transition-metal catalysts with variable chemical states are more effective in activating PMS (Peng et al., 2021; Zheng et al., 2019). Zheng et al. found that the ATZ removal degree reached 96.0% within 40.0 min in PS-Fe$_2$O$_3$/PMS system (Zheng et al., 2019). Peng et al. found that Co$_3$O$_4$@NSC efficiently activated PMS to degrade paracetamol (Peng et al., 2021). Recent years, transition-metal sulfides (TMS) have drawn great attention in environmental remediation due to its rich redox sites, excellent electrical conductivity and catalytic performance (Li et al., 2021b). Among them, FeS$_x$ is considered to be a potential catalyst for organic pollutant degradation by activating PMS due to its low toxicity. Xu et al. found that 100.0% of ciprofloxacin and norfloxacin were degraded within 120.0 min by the FeS/PMS system (Xu and Sheng, 2021).

Metal-organic frameworks (MOFs) are composed of the metal nodes/clusters and organic ligands with large specific surface area (Fu et al., 2021), high porosity and open crystalline structure, which are widely applied in catalysis (Wang et al., 2022c; Zhao et al., 2022a, 2022b), adsorption (Li et al., 2022c; Ren et al., 2022; C. Wang et al., 2022a) and sensor (Wang et al., 2021). TMS derived from MOFs are widely used in environmental remediation due to their tunable morphology and pore size as well as large specific surface area (Du et al., 2022; Hang et al., 2022). MIL-88A(Fe), a typically Fe-based MOF, is synthesized from Fe^{3+} and fumaric acid (Wang et al., 2022d). Although MIL-88A(Fe) can be applied to SR-AOP to degrade contaminants due to its environmental friendliness, the poor-stability limits its application (Yi et al., 2021). Nowadays, metal oxides and metal-carbon composites with high stability derived from MIL-88A(Fe) have been widely used to activate PMS/PDS to remove organic pollutants (Li et al., 2020; Zhang et al., 2021b). For example, Zhang et al. prepared M−Fe$_3$O$_4$-600@PBS using MIL-88A(Fe) as precursors for tetracycline (TC) degradation, in which 97.5% of TC was degraded within 40.0 min in M−Fe$_3$O$_4$-600@PBS/PDS system under white light irradiation (Zhang et al., 2021b). Similarly, Li et al. synthesized Fe$_x$C−600 derived from MIL-88A(Fe) that exhibited excellent phenol degradation performance (Li et al., 2020). However, work related to the removal of organic pollutants by metal-sulfides derived from MIL-88A(Fe) for PMS/PDS activation has not been reported.

Low conversion from Fe^{3+} to Fe^{2+} is a major problem that severely limits the removal degree of organic pollutants in the Fe(II)/PMS system (Lan et al., 2022; Sheng et al., 2019). Thus, the improvement of the activation efficiency of PMS can be achieved by enhancing the conversion between Fe^{3+} and Fe^{2+}. Xing's group reported that MoS$_2$ could be used as a cocatalyst to accelerate the cycling of Fe^{3+}/Fe^{2+}, boosting the pollutants removal degree (Chen et al., 2022; Du et al., 2020).

Additionally, MoS$_2$ can also activate PMS to degrade pollutants in a certain degree (Nie et al., 2022). We believe that constructing a heterogeneous interface between MoS$_2$ and FeS$_x$ derived from MIL-88A(Fe) would be an effective method to improve the removal degree of organic pollutants via PMS activation.

Therefore, a series of FeS$_x$@MoS$_2$-x (FM-x) composites derived from MIL-88A were synthesized through a facile two-step method (Scheme 1), which were applied to degrade ATZ by activating PMS. The synergistic mechanism between FeS$_x$ and MoS$_2$ was investigated in FM-0.96/PMS/ATZ system. Furthermore, the catalytic mechanism was proposed, and the degradation pathways as well as toxicological analysis were deduced. Importantly, a fixed membrane reactor was fabricated based on FM-0.96 powder catalysts for continuous-flow wastewater treatment. This work provides a strategy for the preparation of a catalyst with efficient SR-AOP catalytic performance and long-term operation.

2. Experimental

The details of chemical reagents, characterization methods and experimental processes are provided in the Supplementary Information (SI).

2.1. Synthesis of MIL-88A(Fe)

The precursor of spindle-shaped MIL-88A(Fe) was prepared by a solvothermal method (Yi et al., 2021). Typically, fumaric acid (0.580 g) and FeCl$_3$·6 H$_2$O (1.352 g) were dissolved in DMF (50.0 mL) by stirring for 1.0 h in a 100.0 mL Teflon-lined, and then heated at 100 °C for 12.0 h. After cooling down to room temperature, the as-synthesized MIL-88A(Fe) was washed with DMF and absolute ethanol, and dried at 60 °C overnight.

2.2. Synthesis of FeS$_x$@MoS$_2$-x (FM-x) composites

Firstly, 0.10 g MIL-88A(Fe) and 0.85 g thiourea were dissolved into 15.0 mL ultrapure water, then a certain amount of ammonium molybdate tetrahydrate was added into the above solution. After stirring for 10.0 min, the mixture was sealed in a 25.0 mL Teflon-lined and heated at 180 °C for 24.0 h. Finally, the FeS$_x$@MoS$_2$ (FM-x) composites were collected after centrifugation, washing and drying. The composites were named as FM-x (x = 0.54, 0.96, 3.22, 5.05 represent the real molybdenum/iron content ratios determined by ICP-OES). The individual FeS$_x$ and MoS$_2$ were synthesized without the addition of ammonium molybdate tetrahydrate and MIL-88A(Fe), respectively.

2.3. SR-AOP catalytic activity tests

Batch experiments were conducted in a 55.0 mL flask under dark condition. Briefly, the degradation experiments were conducted by adding 0.15 mM PMS to the 10.0 mg/L ATZ solution with 0.2 g/L catalyst. At pre-set time intervals, 1.5 mL ATZ solution was taken out, filtrated and immediately quenched with 10.0 μL methanol for the determination of ATZ concentration. It was frankly that some uncertainties might occur in sampling within such a short time interval as the first 0.5 min. Therefore, three parallel experiments were performed to reduce the uncertainty. Detailed information on analytical methods can be found in SI.

2.4. Continuous operation experiment

Continuous operation of ATZ degradation was conducted by using a

homemade fixed membrane reactor. In detail, two concentrations of ATZ solutions (1.0 and 10.0 mg/L) were selected for continuous operation tests. The ATZ solution was delivered by a peristaltic pump (BT100L-CE) at the flow rates of 0.90 L/h, while the PMS solution (250.0 mM) by a high precision injection pump with the injection speed of 0.60 mL/h.

3. Results and discussion

3.1. Characterizations

The powder X-ray diffraction (PXRD) pattern of the as-synthesized MIL-88A is well-matched with the relevant references (Fig. S2) (Yi et al., 2021). The peaks at 8.02°, 10.32° and 12.96°, which were ascribed to (100), (101) and (002) facets of MIL-88A, respectively (Yi et al., 2021). Moreover, the scanning electron microscopy (SEM) image showed that the synthesized MIL-88A exhibited a spindle morphology (Fig. 1b). As shown in Fig. 1a, the peaks of the pristine FeS$_x$ PXRD pattern were consistent with the Fe$_3$S$_4$ (PDF#97-004-2491) and FeS$_2$ (PDF#97-003-5010). For the pure MoS$_2$ PXRD pattern, the main peaks at 14.26°, 28.7°, 32.91° and 58.15° corresponded to the (002), (004), (100) and (110) planes, respectively, which matched well with the standard card (PDF#01–075–1539). For the FM-x composites, the main peaks of both FeS$_x$ (FeS, FeS$_2$ and Fe$_3$S$_4$) and MoS$_2$ could be observed, indicating that FM-x composites were successfully prepared. With the mass ratio of ammonium molybdate to MIL-88A increased, the crystallinity of FM-x composites became worse, which could be attributed to the low crystallinity of MoS$_2$. The SEM image showed that FM-0.96 exhibited a flower-like morphology with particle size in the range of 500 nm ~ 600 nm (Fig. 1c). It could be seen that a layer of FeS$_x$ had been deposited on the surface of MoS$_2$ (Fig. 1d), indicating the formation of heterogeneous interface between FeS$_x$ and MoS$_2$. EDS elemental mappings (Fig. 1e-h) confirmed the structural features of FM-0.96 as revealed by the SEM and TEM image mentioned above. In addition, the HRTEM of FM-0.96 showed that the fringe spacings of 0.165, 0.221 and 0.276 nm could be assigned to the (020) crystalline facet of FeS, (121) crystalline facet of FeS$_2$ and (100) crystalline facet of MoS$_2$ respectively, demonstrating the formation of heterogeneous junction between FeS$_x$ and MoS$_2$ (Fig. 1i) (Peng et al., 2022). The inset SAED image of Fig. 1i showed that the diffraction rings of (020), (121) and (100) could be ascribed to FeS, FeS$_2$ and MoS$_2$ crystals, respectively, which further supported the HRTEM results. For the electrochemical impedance spectroscopy (EIS), the semicircular of FM-0.96 was smaller than those of the pure FeS$_x$ and MoS$_2$, further verifying the formation of heterogeneous junction and the electron transfer between the individual

components (Fig. 1j) (Chen et al., 2021b; Wang et al., 2022b). The N$_2$ adsorption–desorption isotherm and pore size distribution of FM-0.54, FM-0.96, FM-3.22 and FM-5.05 displayed the type IV isotherm (Fig. S3a). And the pore sizes of FM-0.54, FM-0.96, FM-3.22 and FM-5.05 were 2 nm ~ 50 nm (Fig. S3b). The above results indicated the meso-porous characteristic of FM-x composites. The specific surface area and pore volume were shown in Table S1. The specific surface area of FM-0.54, FM-0.96, FM-3.22 and FM-5.05 were 16.33, 8.28, 4.23 and 3.62 m^2/g, respectively. These results indicated that the increase of Mo content leads to surface agglomeration, resulting in blockage of the pores and reduction of specific surface area.

3.2. The growth mechanism of FeS$_x$, MoS$_2$ and FM-0.96

When the mixed aqueous solution of MIL-88A and thiourea was sealed in a Teflon-lined reactor for hydrothermal reaction at 180 °C, the released sulfide ions from thiourea could react with the Fe^{3+} in MIL-88A to form small FeS$_x$ particles (Fig. 2a and Fig. S4a). This process was consistent with the previous literature (Geng et al., 2022). With the prolonged reaction time, the small FeS$_x$ particles was gradually assembled into microspheres (Fig. 2b-c) and plate-like morphology (Fig. 2d).

When the mixed aqueous solution of thiourea and ammonium molybdate tetrahydrate was sealed in a Teflon-lined reactor for hydrothermal reaction at 180 °C, the small nanospheres of MoS$_2$ were firstly formed after 1.0 h (Fig. 2e), which gradually grew larger as time went on (Fig. 2f–h).

When MIL-88A, thiourea and ammonium molybdate tetrahydrate all presented under the identically hydrothermal condition, both the reaction between the MIL-88A and thiourea to generate small FeS$_x$ particles and the formation of MoS$_2$ occurred within 1 ~ 3 h (Fig. 2i-j and Fig. S4b). Subsequently, MoS$_2$ gradually grew into larger flower-like morphology, and the formed small FeS$_x$ particles derived from MIL-88A was deposited on the surface of the MoS$_2$ (Fig. 2k-l), which impeded the assemble and morphology transformation of FeS$_x$ particles. The HAADF-EDS lines of FM-0.96 demonstrate that FeS$_x$ uniformly covered on the surface of MoS$_2$, verifying the growth mechanism mentioned above (Fig. S5). More importantly, the FeS$_x$ particles uniformly deposited on the MoS$_2$ surface promoted the formation of rich heterogeneous interface, which would improve the catalytic performance significantly. In addition, FeS$_x$-MoS$_2$ composites (namely FM-iron salts) were prepared by replacing MIL-88A (Fe) with FeCl$_3$·6H$_2$O (Detailed characterization analysis of FM-iron salts could be found in SI). The k value of the FM-0.96/PMS system was 10 times higher than that of the FM-iron salts/PMS system (Fig. S6), demonstrating that MOF self-sacrificing method facilitates the tight combination between FeS$_x$
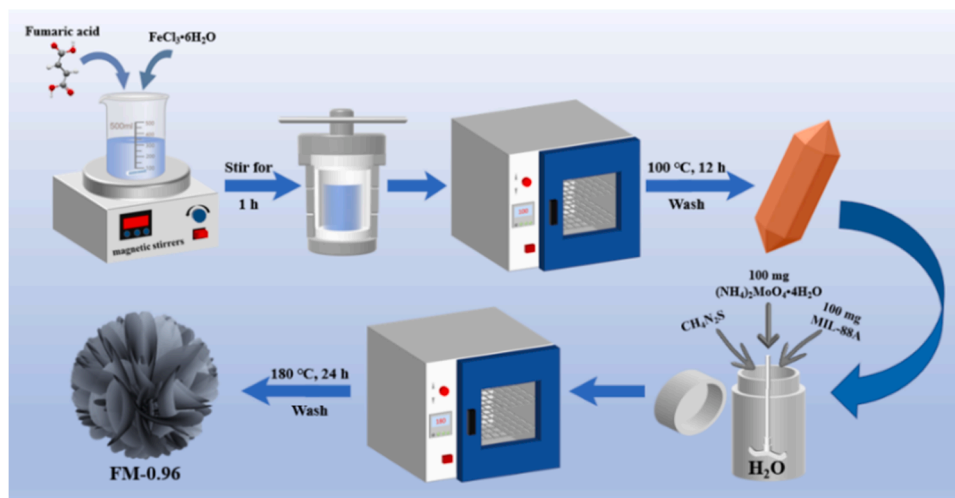
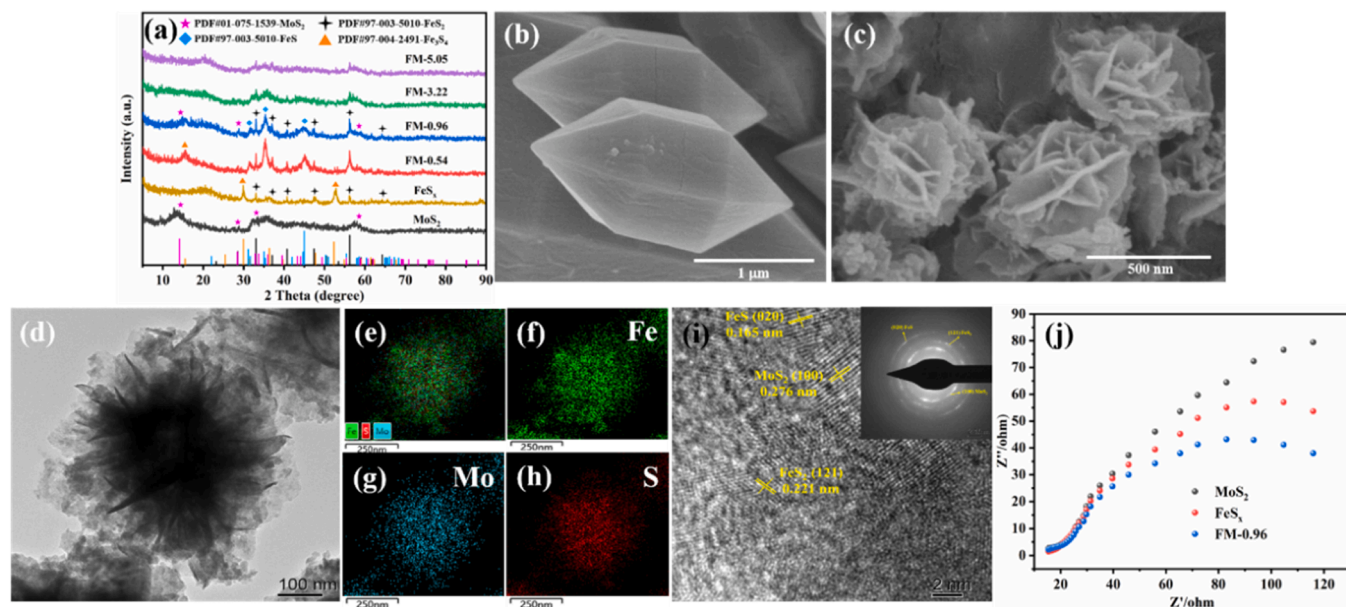**Scheme 1.** Illustration of the fabrication process of FM-0.96.

Fig. 1. (a) The PXRD patterns of as-prepared catalysts. The SEM images of (b) MIL-88A, (c) FM-0.96. The TEM image of (d) FM-0.96. (e-h) The EDS elemental mapping images of FM-0.96. (i) The HRTEM image of FM-0.96 (inset SAED image of FM-0.96). (j) Electrochemical impedance spectroscopy analysis of MoS_2, FeS_x and FM-0.96.
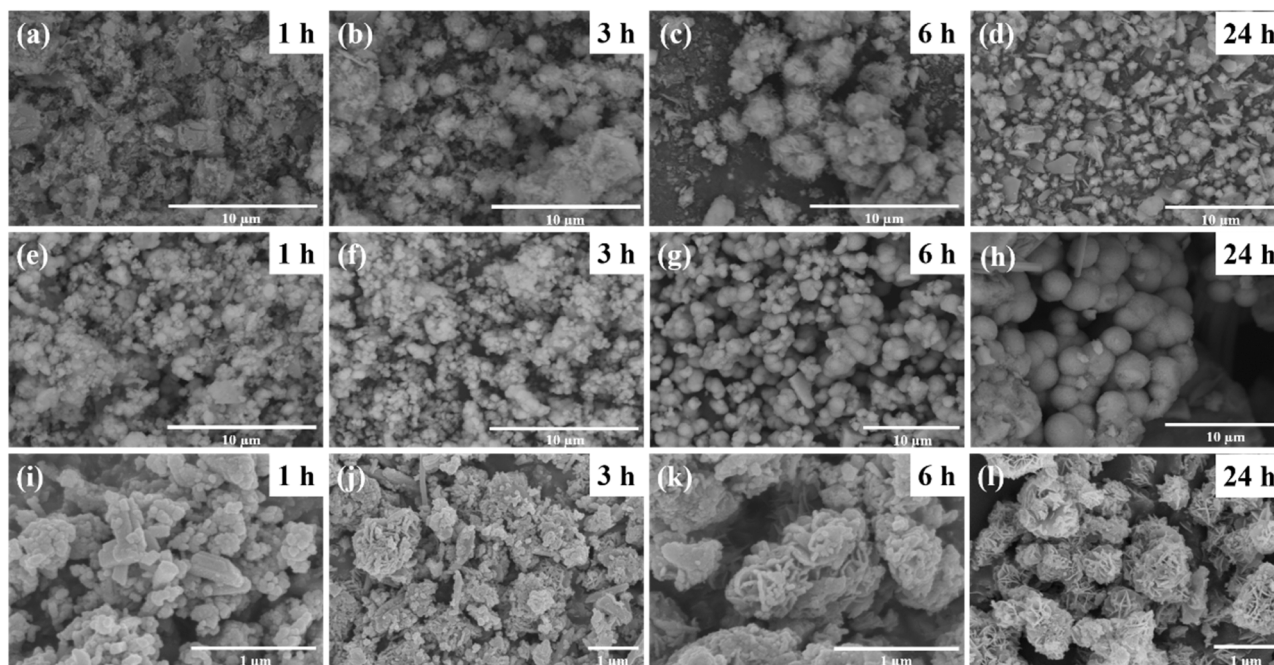

Fig. 2. The SEM images of (a–d) FeS_x, (e-h) MoS_2, (i-l) FM-0.96 at different reaction time.

and MoS_2, leading to a stronger interfacial interaction, greatly boosting the catalytic performance.

3.3. ATZ degradation performance over FM-0.96

The ATZ removal degrees were about 2% and 3% within 6.0 min by individual PMS and FM-0.96, respectively (Fig. 3a). The ATZ removal degrees of pristine FeS_x and MoS_2 on activating PMS were not ideal, which just reached 66.8% and 17.5%, respectively. ATZ removal degree was significantly improved in the FM-x/PMS system. The ATZ removal degrees of FM-0.54, FM-0.96, FM-3.22 and FM-5.05 were 93.3%, 99.2%, 98.4% and 97.9%, respectively. Meanwhile, the reaction rate constant *k*

values of different catalysts were calculated, as depicted in Fig. 3b. Compared to FeS_x/PMS and MoS_2/PMS systems, the *k* value of FM-0.96 was increased by about 40 and 320 times, respectively, which could be ascribed to the synergistic effect between FeS_x and MoS_2 (Lu et al., 2021; Wu et al., 2021). The ATZ removal degree of the physical mixture of FeS_x and MoS_2 with a mass ratio of 0.96 just reached 67.5% within 6.0 min (Fig. 3c), further demonstrating the strong synergistic effect between individual components of FM-0.96. From the perspective of the ATZ removal degree and rate, FM-0.96 was selected to further experiments.

As shown in Fig. 3d, the ATZ removal degree in FM-0.96/PMS system was 100.0% within 6.0 min, which was higher than those of the FM-0.96/hydrogen peroxide (H_2O_2) system (9.0%) and the FM-0.96/
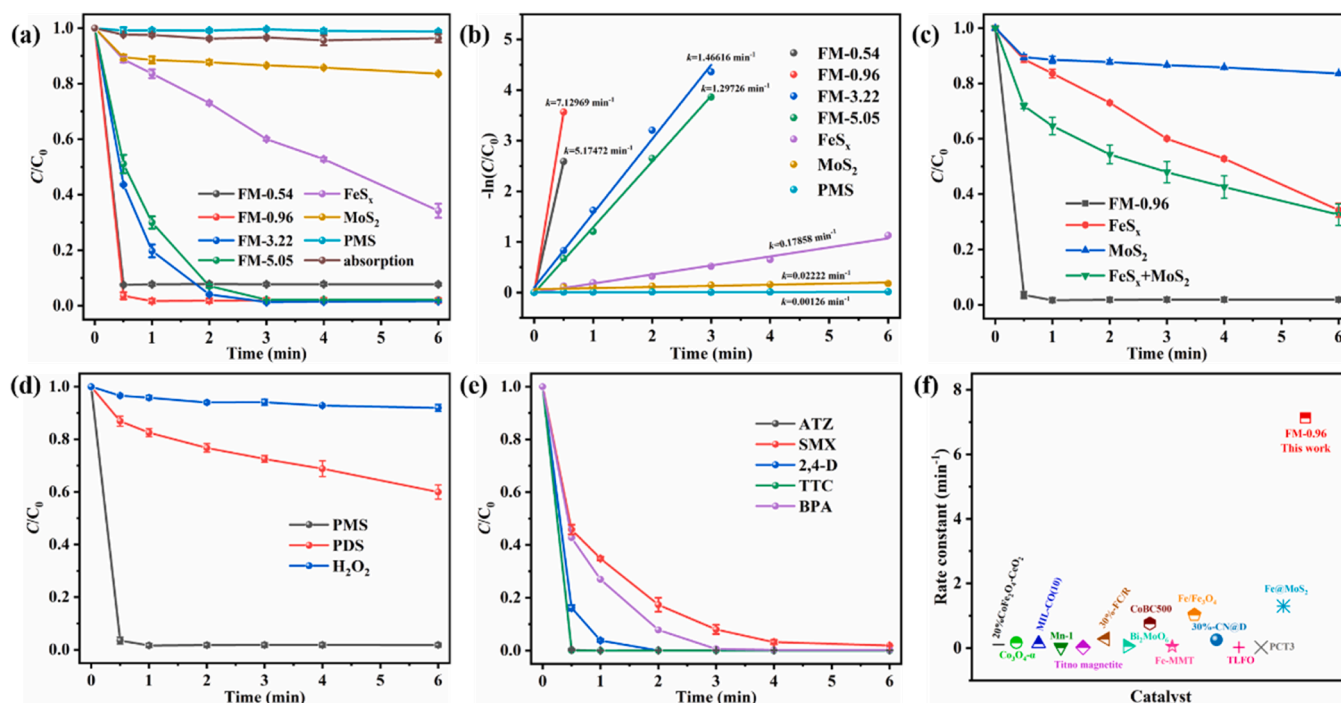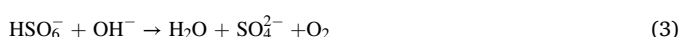
Fig. 3. (a) The removal degree of ATZ in different systems. (b) The *k* values in different systems. (c) The control experiments on ATZ removal degree in different systems. (d) Effect of oxidants on ATZ removal by FM-0.96. (e) The removal degree of SMX, BPA, TTC, ATZ and 2,4-D by FM-0.96. (f) The comparison of rate constant of different catalysts (Dong et al., 2020; Hu et al., 2021; Lai et al., 2020; Li et al., 2022; Liu et al., 2020; Lu et al., 2022; Roy et al., 2022; Shen et al., 2020; Sun et al., 2021a; Sun et al., 2021b; Tang et al., 2022; Wang et al., 2020; Wei et al., 2022; Zeng et al., 2020). Reaction conditions: ATZ = 10.0 mg/L, SMX = 10.0 mg/L, 2,4-D = 10.0 mg/L, BPA = 10.0 mg/L, TTC = 10.0 mg/L, PMS = 0.1 mM, Catalyst = 0.2 g/L, initial pH = 5.8, PMS/ATZ molar ratio = 3.25.

peroxydisulfate (PDS) system (41.0%), possible originating from the spatial hindrance effect of PDS and the higher O-O bond energy of H_2O_2 (Huo et al., 2020; Li et al., 2018a). Fig. 3e illustrates the removal of several contaminants by FM-0.96 via PMS activation. It can be observed that more than 98.0% removal degrees were achieved within 6.0 min for the degradation of ATZ, sulfamethoxazole (SMX), bisphenol A (BPA), tetracycline (TTC) and 2,4-Dichlorophenoxyacetic acid (2,4-D), indicating FM-0.96 can effectively remove different kinds of pollutants. To further verify the excellent catalytic performance of FM-0.96, the comparison by using the rate constant as the evaluation index with previously reported catalysts for ATZ degradation was performed, as shown in Fig. 3f and Table S2. The ATZ removal rate constant of FM-0.96 was higher than that of a majority of catalysts (more details can be found in Table S2), which demonstrates the excellent catalytic performance of FM-0.96.

3.4. Effect of key factors on ATZ degradation

3.4.1. Effect of pH

To examine the influence of pH on the reaction system, activity experiments were conducted at different initial pH (ranging from 2.0 to 9.0). As shown in Fig. 4a, the complete ATZ removal was achieved in the pH range of 4–8 within 6.0 min, and the ATZ removal degree was inhibited at pH 2.0 (84.5%) and 9.0 (69.2%). The PXRD patterns of FM-0.96 after reaction under pH 2.0 changed obviously (Fig. S7), demonstrating that the low removal degree of FM-0.96 at pH 2.0 might be due to its instability. Under pH 9.0, the Fe^{2+} of FM-0.96 was partially passivated and PMS self-decomposition to form SO_4^{2-} and O_2 (Eqs. (1)–(3)), reducing the ATZ removal degree (Lu et al., 2021).

$$HSO_5^- + H_2O \rightarrow SO_5^{2-} + H_3O^+ \tag{1}$$

$$HSO_5^- + SO_5^{2-} \rightarrow HSO_6^- + SO_4^{2-} \tag{2}$$

$$HSO_6^- + OH^- \rightarrow H_2O + SO_4^{2-} + O_2 \tag{3}$$

3.4.2. Effect of PMS/ATZ molar ratios and ATZ concentrations

The PMS/pollutant molar ratio is becoming a way to evaluate the excellent catalytic performance of different catalysts in the SR-AOP process in recent years (Li et al., 2019a). As shown in Fig. 4b, the ATZ removal degree increased with the increasing of the PMS/ATZ molar ratio, and reached 100.0% when the ratio was 3.25. The results indicated that with the increase of PMS dosage, more ROS could be generated, beneficial to the enhancing of the ATZ degradation. However, the ATZ removal degree was not obviously enhanced with the increase of PMS/ATZ molar ratio from 3.25 to 4.68, which might be due to the self-quenching effect of excessive PMS (Eqs. (4)–(5)) (Wang et al., 2022b). In addition, the total organic carbon (TOC) removal degrees were investigated under the different PMS/ATZ molar ratios (Table 1). It can be clearly seen that 40.0% TOC removal degree was achieved with the PMS/ATZ molar ratio of 3.25, which was highest compared to the other three PMS/ATZ molar ratios. As shown in Table 1, FM-0.96 exhibited excellent catalytic performance on ATZ degradation with a smaller PMS/ATZ molar ratio compared to other catalysts.

$$SO_4^{\cdot-} + SO_4^{\cdot-} \rightarrow S_2O_8^{2-} \tag{4}$$

$$HSO_5^- + SO_4^{\cdot-} \rightarrow SO_5^{\cdot-} + SO_4^{2-} + H^+ \tag{5}$$

Effect of ATZ concentrations were also investigated in FM-0.96/PMS system. As shown in Fig. 4c, the ATZ removal degrees in FM-0.96/PMS system were 100.0%, 100.0%, 100.0% and 97.0% when ATZ concentrations were 1.0, 5.0, 10.0 and 20.0 mg/L, respectively, further indicating the excellent catalytic performance of the FM-0.96 toward ATZ degradation.

3.4.3. Effect of temperature

There are several steps during the ATZ degradation process in FM-0.96/PMS system. Firstly, PMS diffused toward the surface of the
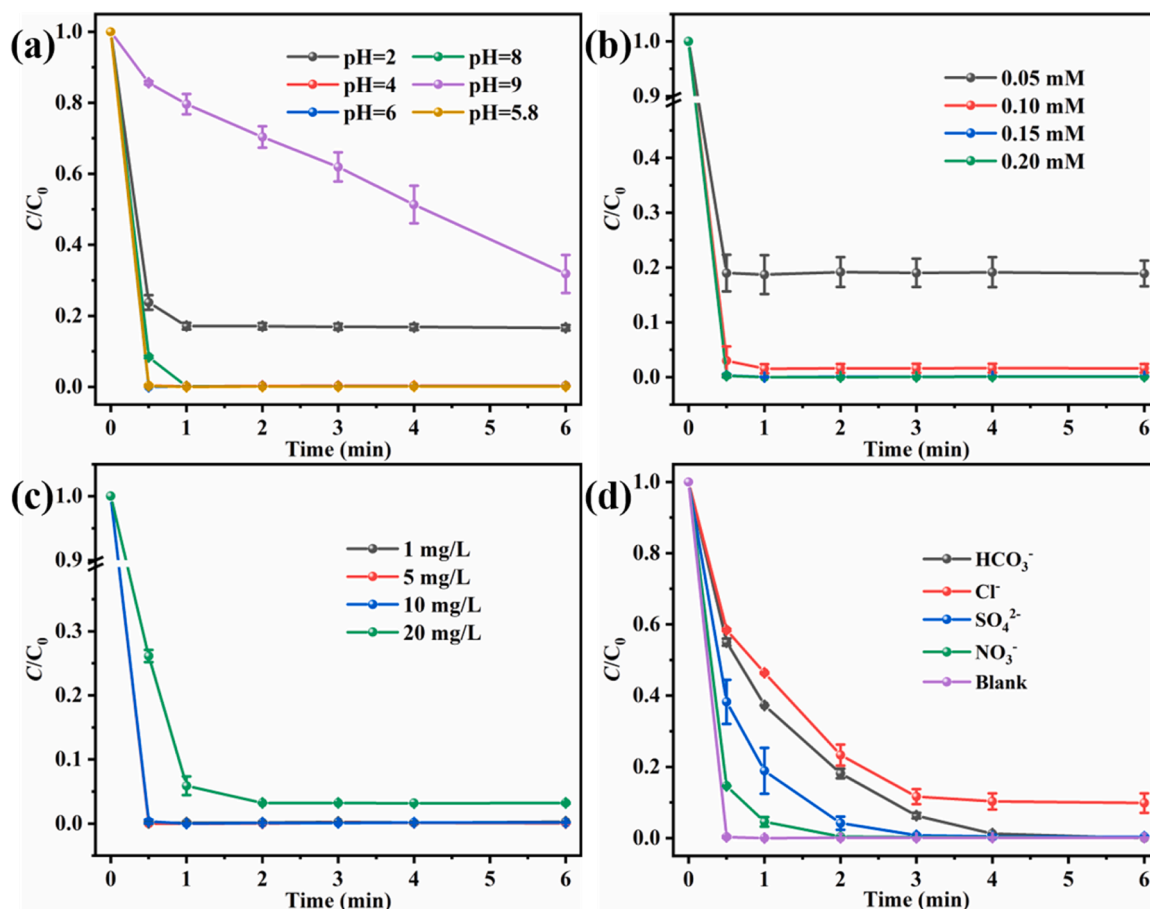
Fig. 4. Effects of (a) initial pH, (b) PMS concentration, (c) ATZ concentration and (d) inorganic anions on ATZ degradation. Reaction conditions: ATZ = 10.0 mg/L, PMS = 0.15 mM, catalyst = 0.2 g/L, pH = 5.8.

catalyst, and was activated by the superficial active sites like Fe^{2+} to generate ROSs ($\cdot$OH, SO_4^{2-}, etc) and Fe^{3+}. Then, ATZ diffused and reacted with the generated ROSs to form intermediates, in which the intermediates further reacted with the ROSs to produce CO_2 and H_2O, or diffused away from the catalyst surface. Finally, Mo^{4+} could react with Fe^{3+} to regenerate Fe^{2+}. In short, the ATZ degradation process involved diffusion and chemical reactions. To verify whether the high reaction rate constant for ATZ removal in FM-0.96/PMS system was dominated by mass transfer or chemical reaction, the ATZ (20.0 mg/L) degradation experiments at different temperature of 278 K, 283 K and 288 K were conducted (Fig. S8). As the temperature increases, the ATZ removal degrees were enhanced obviously. Based on above results, the activation energy (E_a) was calculated using the Arrhenius equation (Eq. (6)) (Zhao et al., 2021).

$$\ln k = \ln A - E_a/RT \qquad (6)$$

Where, k is the reaction rate constant for the ATZ degradation; A denotes the pre-exponential factor ($\min^{-1}$); R is 8.314 J mol^{-1} K^{-1} (the universal gas constant) and T represents the temperature (K). The E_a calculated from the ATZ degradation in FM-0.96/PMS system was 71.12 kJ/mol, indicating that the catalytic process could not be controlled by the mass transfer (the E_a of diffusion-controlled was 10–13 kJ/mol), which was consistent with the previous reported literature (Zhao et al., 2021). The mass ratio Mo/Fe in the FM-x affected the catalytic performance significantly, as shown in Fig. 3a. With the increase of the Mo/Fe ratio, the ATZ removal degree firstly increased then decreased, and reached the highest at the ratio of 0.96, suggesting that the Fe^{2+} regeneration by Mo^{4+} was the crucial factor for the improved catalytic performance.

3.4.4. Effect of co-existing anions

In the SR-AOP process, the anions normal existed in polluted water, such as HCO_3^-, Cl^-, SO_4^{2-} and NO_3^-, would affect the degradation of pollutants. Therefore, it was essential to investigate the influence of the mentioned above common anions (Table S3) on ATZ degradation in the FM-0.96/PMS system.

With the addition of HCO_3^-, SO_4^{2-}, NO_3^- and Cl^-, the ATZ degradation rates were inhibited due to the reaction between these inorganic ions and free radicals like $\cdot$OH and $\cdot SO_4^-$ (Du et al., 2022a; Li et al., 2022a), as showed in Fig. 4d. And the most obvious inhibition of ATZ degradation rate was observed when Cl^- was added. As reported previously, Cl^- can scavenge sulfate radicals and hydroxyl radicals to generate chlorine-reactive species such as $Cl\cdot$ and $Cl_2\cdot^-$ (2.4 V and 2.0 V vs NHE) (Eqs. (7)–(9)) (Du et al., 2022a), which have lower redox potential than $\cdot$OH (1.8–2.7 V vs NHE) and $SO_4\cdot^-$ (2.5–3.1 V vs NHE), leading to an inhibitory effect on ATZ degradation. In all, above results demonstrate the feasible application of FM-0.96 in practical water treatment.

$$SO_4\cdot^- + Cl^- \rightarrow SO_4^{2-} + Cl\cdot \qquad (7)$$

$$\cdot OH + Cl^- \rightarrow OH^- + Cl\cdot \qquad (8)$$

$$Cl\cdot + Cl^- \rightarrow Cl_2\cdot^- \qquad (9)$$

3.5. Catalytic ATZ degradation mechanism via activating PMS over FM-0.96

3.5.1. Identification of ROS in FM-0.96 system

Activation of PMS has been reported for both free radicals ($SO_4\cdot^-$,

Table 1
Summary of the molar ratio of PMS/ATZ in SR-AOP processes.

Catalyst	Catalyst dosage (g/L)	ATZ concentration (mg/L)	PMS concentration (mM)	PMS/ATZ molar ratio	Radiation source	Time (min)	Removal degree (%)	TOC removal degree	Ref
TiO$_2$@LaFeO$_3$	0.4	2.5	0.2	17.24	Vis	90.0	100.0	37.04	(Wei et al., 2022)
30 %−FC/R	0.3	10.0	0.5	10.8	Dark	20.	90.44	–	(Sun et al., 2021b)
PCT3	0.4	10.0	0.33	7.13	Vis	60.0	75.0	46.08	(Tang et al., 2022)
Fe−15 %C	0.06	10.784	0.25	5.0	Dark	120.0	91.6	–	(Li et al., 2021a)
Fe@MoS$_2$	0.1	8.6272	0.5	12.5	Dark	10.0	100.0	–	(Sun et al., 2021a)
CoFe$_2$O$_4$	0.4	10.0	0.8	8.64	Dark	30.0	99.0	27.0	(Li et al., 2018b)
ECM−Co−NZ	0.3	10.0	0.5	3.5997	Dark	14.0	100.0	–	(Ji et al., 2019)
MLCMO	0.1	2.1568	1.0	50.0	Dark	30.0	97.0	37.0	(Luo et al., 2019)
Mn−1	0.25	10.784	3.0	120.0	Dark	60.0	74.2	51.0	(Zeng et al., 2020)
Co$_3$O$_4$	0.4	4.3136	2.0	166.66	Dark	15.0	99.0	–	(Fan et al., 2017)
CoBC500	0.1	2.1586	1.0	50.0	Dark	6.0	99.0	–	(Liu et al., 2020)
Bi$_2$MoO$_6$	0.6	2.5	0.8	23.02	Vis	60.0	99.0	–	(Shen et al., 2020)
PS-Fe$_2$O$_3$-2	0.4	1.0784	0.6	60.0	Dark	40.0	96.0	–	(Zheng et al., 2019)
MIL-CO (10)	0.01	10.0	0.42	18.14	Vis	60.0	99.9	78.5	(Roy et al., 2022)
FM−0.96	0.2	10.0	0.05	1.17	Dark	6.0	81.1	5.0*	This work
FM−0.96	0.2	10.0	0.1	2.34	Dark	6.0	98.3	18.0*	This work
FM−0.96	0.2	10.0	0.15	3.25	Dark	1.0	100.0	40.0*	This work
FM−0.96	0.2	10.0	0.2	4.68	Dark	1.0	100.0	38.0*	This work

Notes: "−" means not mentioned in the literature. "* " means TOC removal degree within 60.0 min.

·OH, and O$_2$·$^-$) and non-radicals (^{1}O$_2$ and high-valent metal) pathways. So far, the generation mechanism of active species in the SR-AOPs is still controversial. In our work, several scavengers were selected as ROS quenching reagents. Typically, free radicals like SO$_4$·$^-$, ·OH and O$_2$·$^-$ can be quenched by adding methanol, t-butanol (TBA) and benzoquinone (BQ), respectively. As 1.0 mM BQ was added, the ATZ removal degree decreased from 100.0% to 95.0%, indicating that O$_2$·$^-$ played a little role on ATZ degradation (Fig. 5a). Furthermore, when 50.0 mM
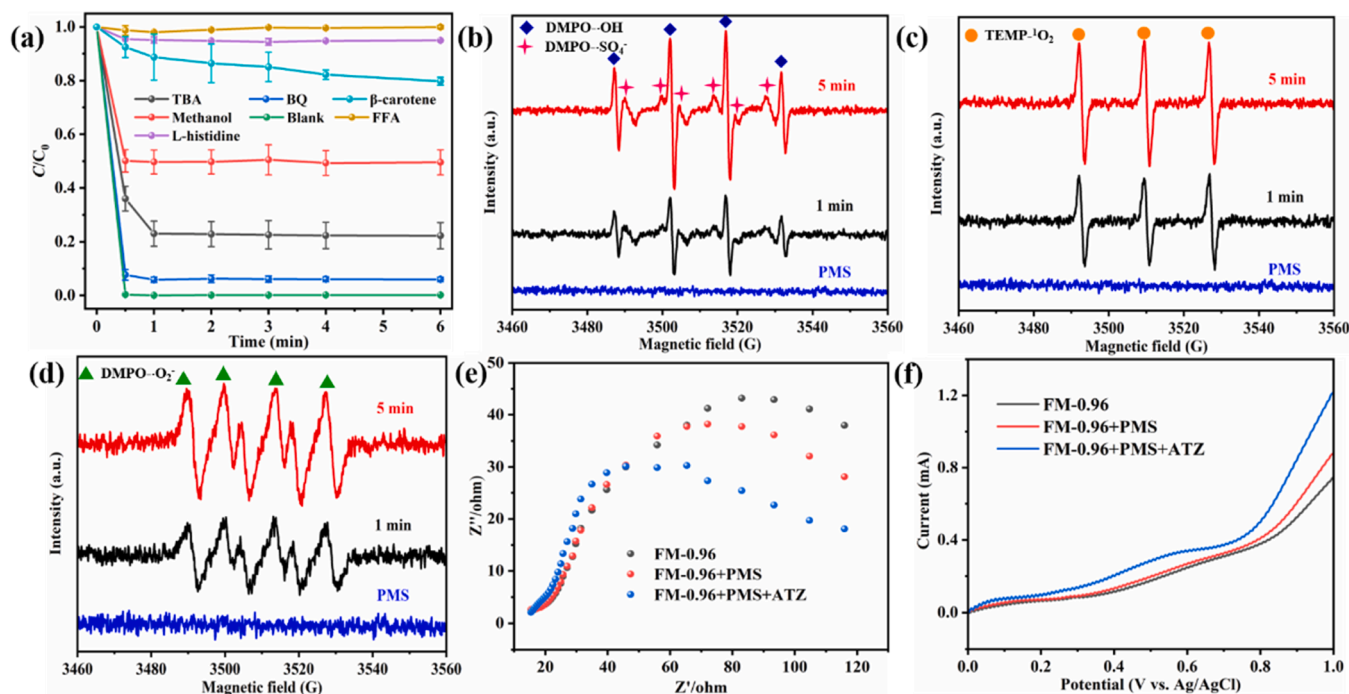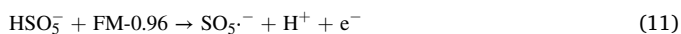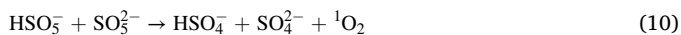

Fig. 5. (a) The quenching experiments on ATZ degradation. ESR spectra of (b) DMPO- SO$_4$·$^-$ and DMPO- ·OH, (c) TEMP-^{1}O$_2$, (d) DMPO- O$_2$·$^-$. (e) Electrochemical impedance spectroscopy analysis of the different catalytic systems. (f) LSV curves in different systems.

TBA and methanol were added, the ATZ removal degrees were decreased from 100.0% to 77.8% and 50.0%, respectively. This phenomenon indicated that $SO_4{\cdot}^-$ and $\cdot OH$ played a significant role in the FM-0.96/ATZ/PMS system. In addition, we verified the role of $^1O_2$ by adding trapping agents (L-histidine, furfuryl alcohol (FFA) and β-carotene) to the FM-0.96/ATZ/PMS system. In the presence of 1.0 mM L-histidine and 50.0 mM FFA, the ATZ removal degrees were inhibited severely, decreasing from 100.0% to 5.0% and 1.0%, indicating that $^1O_2$ might also play a significant role. As reported in literature, FFA and L-histidine, as reducing agents, might induce rapid PMS consumption and could not identify the quenching effect of $^1O_2$ (Yun et al., 2018). Therefore, β-carotene was also selected to quench $^1O_2$ since it hardly reacts with PMS (Wang et al., 2022b). When 0.47 mM β-carotene was added, ATZ removal degree decreased from 100.0% to 21.3%, which suggested that the $^1O_2$ was the main contributor in FM-0.96/PMS/ATZ system. It has been reported that the PMS self-decomposition, dissolved oxygen (DO) and $O_2{\cdot}^-$ could be converted to $^1O_2$ during the PMS activation process. $O_2{\cdot}^-$ would not be source of the $^1O_2$ because of the little inhibitory effect for ATZ degradation, as demonstrated by quenching experiment. Besides, the contribution of PMS self-decomposition to produce $^1O_2$ can be considered negligible due to its very slow reaction rate (Eq. (10)) (Yang et al., 2018). To verify whether DO make a contribution to the $^1O_2$ generation in FM-0.96/PMS/ATZ system, the ATZ solution was purged with nitrogen gas for 10.0 min to eliminate DO from the ATZ solution before the reaction, and nitrogen gas was continuously injected during ATZ degradation. The almost complete degradation of ATZ within 0.5 min in the N_2-saturated FM-0.96/PMS system demonstrates that PMS rather than DO contribute to the formation of $^1O_2$ (Fig. S9). Moreover, PMS can react with FM-0.96 to generate the low reactive $SO_5{\cdot}^-$ (Eq. (11)). On the one hand, $SO_5{\cdot}^-$ reacts with H_2O to from $^1O_2$ (Eq. (12)). On the other hand, $^1O_2$ can be generated through the reaction of excessive $SO_5{\cdot}^-$ (Eq. (13)) (Zhang et al., 2021a). The above results revealed that $^1O_2$ was the dominated ROS in FM-0.96/PMS/ATZ system for PMS activation.

$$HSO_5^- + SO_5^{2-} \rightarrow HSO_4^- + SO_4^{2-} + {}^1O_2 \tag{10}$$

$$HSO_5^- + FM\text{-}0.96 \rightarrow SO_5{\cdot}^- + H^+ + e^- \tag{11}$$

$$2SO_5{\cdot}^- + H_2O \rightarrow 2HSO_4^- + 1.5{}^1O_2 \tag{12}$$

$$SO_5{\cdot}^- + SO_5{\cdot}^- \rightarrow {}^1O_2 + 2SO_4^{2-} \tag{13}$$

To further confirm the above conclusions, electron spin resonance (ESR) was conducted to detect the existence of ROSs with 5, 5-dimethyl-1-pyrroline (DMPO) and 2,2,6,6-Tetramethylpiperidine (TEMP). The signals of DMPO- $SO_4{\cdot}^-$ and DMPO- $\cdot OH$ were observed in FM-0.96/PMS system (Fig. 5b), indicating the presence of $SO_4{\cdot}^-$ and $\cdot OH$. And the signals intensity becomes stronger as time gets long. The presence of signals of DMPO- $O_2{\cdot}^-$ in Fig. 5d for the FM-0.96/PMS system demonstrated the existence rather than the contribution of $O_2{\cdot}^-$ for the ATZ degradation, which was similar to the reported literature (Li et al., 2019b). It can be observed in Fig. 5c that an obvious 1:1:1 triplet-peak signal of TEMP-$^1O_2$ was detected in FM-0.96/PMS system, and the intensity of TEMP-$^1O_2$ signals enhanced as time go on, indicating the presence of $^1O_2$. As depicted in Fig. 5e, the Electrochemical impedance spectroscopy (EIS) curves of FM-0.96/PMS/ATZ system exhibited a smaller semicircular compared to FM-0.96 and FM-0.96/PMS systems, indicating the charge-transfer resistance is lower in the FM-0.96/PMS/ATZ system. Moreover, Linear sweep voltammetry (LSV) experiments (Fig. 5f) showed that the current is very small and almost negligible in the pure FM-0.96 system. Compared to LSV curves in FM-0.96/PMS system, the current increased significantly after adding ATZ, which indicates that the ATZ degradation has occurred over FM-0.96/PMS system. These results illustrate that FM-0.96 was an outstanding catalyst for activating PMS. Furthermore, we use methyl phenyl sulfoxide (PMSO) as the probe to verify the role of high valent Fe

(IV) in FM-0.96/PMS/ATZ system. As described in Fig. S10, the consumption of PMSO is almost as much in the PMS system as in the FM-0.96/PMS system, indicating that the pure PMS can consume PMSO. Meanwhile, the same phenomenon was observed in the generation of methyl phenyl sulfone (PMSO$_2$), which demonstrated that there is no formation of high valent Fe(IV) in FM-0.96/PMS/ATZ system.
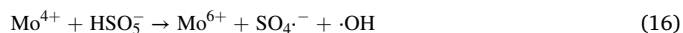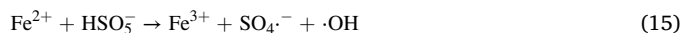
3.5.2. The residual PMS and the generation of $SO_4{\cdot}^-$

The generation of $SO_4{\cdot}^-$ and residual PMS were quantified in FeS$_x$/ATZ/PMS, MoS$_2$/ATZ/PMS and FM-0.96/ATZ/PMS systems. As shown in Fig. 6a, the concentrations of $SO_4{\cdot}^-$ produced within 6.0 min in FeS$_x$/ATZ/PMS and MoS$_2$/ATZ/PMS systems were low, only 1.26 and 1.43 μM, respectively. For the FM-0.96/ATZ/PMS system, the $SO_4{\cdot}^-$ concentration reached 8.94 μM, and generated largely within 0.5 min. Meanwhile, the residual PMS concentration was detected in FeS$_x$/PMS, MoS$_2$/PMS and FM-0.96/PMS systems, as shown in Fig. 6b. The PMS concentration was dropped sharply within 0.5 min in FM-0.96/ATZ/PMS system, which was consistent with the rapid ATZ removal degree. Furthermore, the residual amount of PMS was 0.05, 0.056 and 0.008 mM in FeS$_x$/ATZ/PMS, MoS$_2$/ATZ/PMS and FM-0.96/ATZ/PMS systems within 6.0 min, respectively, which was sufficient for the generation of $SO_4{\cdot}^-$ (Eq. (14)). The result indicating that excess PMS ensure the generation of $SO_4{\cdot}^-$ in FM-0.96/ATZ/PMS system.

$$HBA\ (excess) + SO_4{\cdot}^- \rightarrow hydroquinone + PMS\ (excess) \rightarrow BQ \tag{14}$$
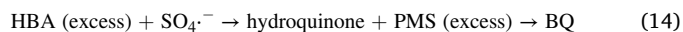
3.5.3. Catalytic mechanism

The XPS analysis was conducted to understand the elemental composition and the chemical state of Fe, Mo and S in the FM-0.96. Notably, it can be seen that the peak at 230.44 eV confirms the presence of Mo-S-Fe bond (Wu et al., 2022), while there is no such peak in pure MoS$_2$ XPS spectra, which demonstrates the formation of strong heterogeneous interface between FeS$_x$ and MoS$_2$ (Fig. 6c). As shown in Fig. 6d, the Fe 2p spectrum of the fresh FM-0.96 was fitted into seven peaks, which coincided with the peaks of Fe^0, Fe^{2+}, Fe^{3+} and satellite peak (Lu et al., 2021). The peak at 708.10 and 720.50 eV could be assigned to Fe^0. In addition, two peaks located at 712.53 and 726.68 eV could be attributed to Fe^{3+}, while the peak at 710.85 and 724.51 eV could be assigned to Fe^{2+}. For the used sample, the percentage of Fe^{3+} decreased from 32.23% to 28.83% after the reaction, indicating that some of Fe^{3+} have been converted to Fe^{2+} (Table S4). This phenomenon might be due to the presence of the Mo-S-Fe bond that facilitates the electron transfer from MoS$_2$ to FeS$_x$, leading to the regeneration of Fe^{2+}. The Mo 3d spectra was fitted well into seven characteristic peaks (Fig. 6e). The peaks centered at 226.53, 230.44 and 235.99 eV belong to S 2s, Mo-S-Fe bond and Mo^{6+} 3d, respectively. The two peaks at 228.91 and 232.38 eV were attributed to the Mo^{4+}. And the other two peaks at 229.46 and 233.12 eV were ascribed to the Mo^{5+}. After ATZ degradation, the percentage of Mo^{6+} and Mo^{5+} had decreased by 3.24% and 0.65% with the increase of the percentage of Mo^{4+} by 9.70%, demonstrating the existence of the conversion of Mo^{6+} and Mo^{5+} to Mo^{4+} (Table S4). In Fig. 6f, the S 2p spectra fitted four characteristic peaks at 161.85, 163.14, 164.37 and 169.19 eV, which were attributed to S^{2-}, S$_2^{2-}$, S$_n^{2-}$ and SO$_x$, respectively. The percentage of S^{2-} and S$_2^{2-}$ decreased from 39.53% and 33.89% to 32.73% and 33.29%, while S$_n^{2-}$ and SO$_x$ increased from 15.39% and 11.17 to 18.01% and 15.96%, respectively (Table S4). The above phenomenon indicates that the Mo-S-Fe bond played a significant role in promoting the conversion of Fe^{3+}, Mo^{5+} and Mo^{6+} to Fe^{2+} and Mo^{4+}, respectively, in the FM-0.96/PMS/ATZ system.

$$Fe^{2+} + HSO_5^- \rightarrow Fe^{3+} + SO_4{\cdot}^- + \cdot OH \tag{15}$$

$$Mo^{4+} + HSO_5^- \rightarrow Mo^{6+} + SO_4{\cdot}^- + \cdot OH \tag{16}$$

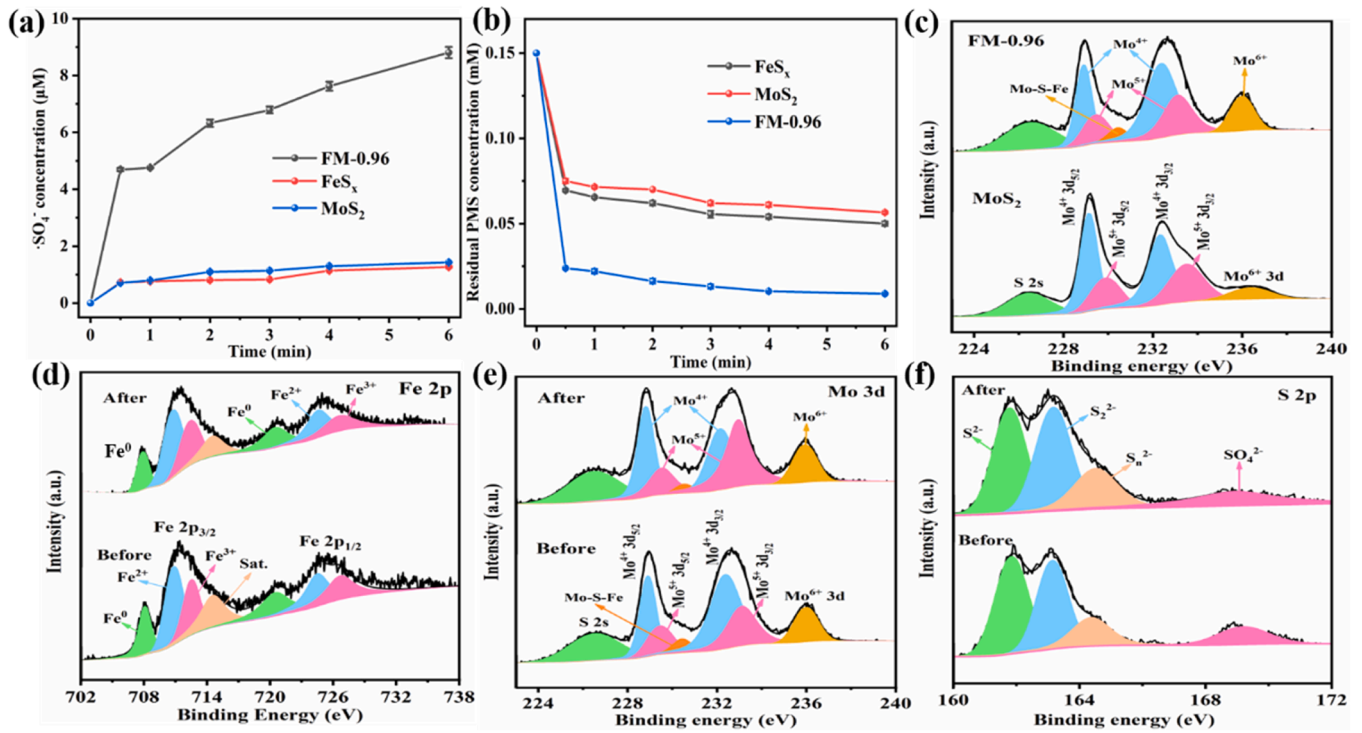$$Mo^{5+} + HSO_5^- \rightarrow Mo^{6+} + SO_4{\cdot}^- + OH^- \tag{17}$$

Fig. 6. (a) The formed $SO_4\cdot^-$ concentrations in difference systems. (b) The residual PMS concentration in difference systems. (c) Mo 3d XPS spectra of FM-0.96 and MoS_2. (d) Fe 2p, (e) Mo 3d and (f) S 2p XPS spectra before and after the degradation reaction. Reaction conditions: PMS = 0.15 mM, Catalyst = 0.2 g/L, initial pH = 5.8, HBA: PMS = 8:1, PMS/ATZ molar ratio = 3.25.
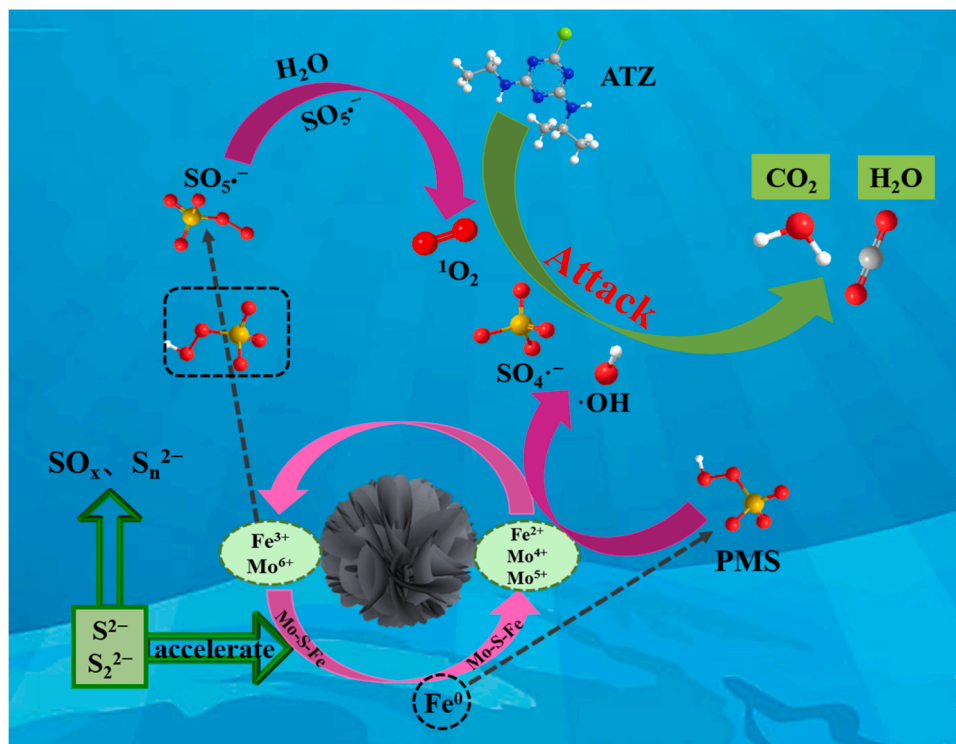
$$Fe^{3+} + HSO_5^- \rightarrow Fe^{2+} + SO_5\cdot^- + H^+ \tag{18}$$

$$Mo^{6+} + HSO_5^- \rightarrow Mo^{4+} + SO_5\cdot^- + H^+ \tag{19}$$

$$Fe^0 + HSO_5^- + H^+ \rightarrow Fe^{2+} + SO_4\cdot^- + H_2O \tag{20}$$

$$Fe^0 + 2Fe^{3+} \rightarrow 3Fe^{2+} \tag{21}$$

$$Fe^0 + 2Mo^{6+} \rightarrow 3Mo^{4+} \tag{22}$$

$$2Fe^{3+} + Mo^{4+} \rightarrow Mo^{6+} + 2Fe^{2+} \tag{23}$$

Fig. 7. The possible catalytic mechanism for ATZ removal in FM-0.96/PMS system.

$$Fe^{3+} + S^{2-}/S_2^{2-} \rightarrow Fe^{2+} + S_n^{2-}/SO_x \quad (24)$$

$$Mo^{6+} + S^{2-}/S_2^{2-} \rightarrow Mo^{4+} + S_n^{2-}/SO_x \quad (25)$$

$$SO_4\cdot^-/\cdot OH/^1O_2 + ATZ \rightarrow intermediates + CO_2 + H_2O \quad (26)$$
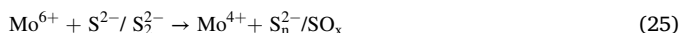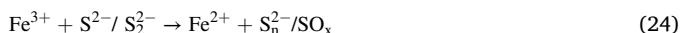
Based on ROS quenching tests, ESR analysis, electrochemical tests and XPS analysis, the catalytic mechanism in FM-0.96/PMS/ATZ system is proposed. As depicted in Fig. 7, the transition metallic redox pairs (Fe^{2+}/Fe^{3+} and $Mo^{4+}/Mo^{5+}/Mo^{6+}$) firstly react with PMS to produce $SO_4\cdot^-$, $\cdot OH$ and $SO_5\cdot^-$ radicals (Eqs. (15)–(19)). Moreover, Fe^0 can also react with PMS to form $SO_4\cdot^-$ in FM-0.96/PMS/ATZ system (Eq. (20)). Simultaneously, Fe^0 and Fe^{3+} promote the regeneration of Fe^{2+} and Mo^{4+} through electron transfer (Eqs. (21)–(23)). Furthermore, the sulfur species could react with Fe^{3+} and Mo^{6+} to generate Fe^{2+} and Mo^{4+} (Eqs. (24)–(25)). In addition, the generated $SO_5\cdot^-$ radicals will continue to react with H_2O and $SO_5\cdot^-$ to form $^1O_2$ (Eqs. (11)–(13)). In all, the free radical ($SO_4\cdot^-$ and $\cdot OH$) and non-free radical ($^1O_2$) pathways contribute to the ATZ degradation (Eq. (26)).

3.6. Possible degradation pathways of ATZ and toxicity analysis

DFT calculation of Fukui function was carried out to calculate the reactive sites to confirm the pathway of ATZ under the ROS attack in FM-0.96/PMS/ATZ system. In this work, the primary ROS are $SO_4\cdot^-$, $\cdot OH$ and $^1O_2$, which are electrophilic species (Chen et al., 2021a), thus Fukui index representing electrophilic attack (f^-)radical attack (f^0) were calculated (Fig. 8c). The natural population analysis (NPA) charge was selected to evaluate the electron activity (Wang et al., 2022d). The geometrical optimization of the molecule and vibrational frequencies calculations were conducted using the B3LYP method with a 6–31+G (d) basis set. Fig. 8a showed the final structure optimized of ATZ by Gaussian 09W software. Typically, the highest occupied molecular orbital (HOMO) is easily to lose electrons, which is of the highest possibility to be attacked by $SO_4\cdot^-$, $\cdot OH$ and $^1O_2$. As exhibited in Fig. 8b, the highest occupied molecular orbital (HOMO) distributions of ATZ are consistent with the active sites obtained from Fukui index results. The reactive sites with large Fukui values indicated higher reactivity. It can be clearly seen that the Cl4 (f^-/f^0 = 0.09012/0.11852), N7 (f^-/f^0 = 0.2132/0.1769), N8 (f^-/f^0 = 0.2276/0.1368), N20 (f^-/f^0 = 0.1578/0.1002) with high Fukui index, which can be attacked by ROS. Therefore, the decomposition of ATZ is mainly carried out on N7, N8, N20 and Cl4, leading to the formation of ATZ^+ and the bond-cleavage of C-N and C-Cl (Wu et al., 2018).

In combination with the Fukui function and LC-MS intermediate products analysis, four pathways of ATZ degradation were proposed and displayed in Fig. 9. The ATZ degradation pathways mainly include dechlorination-hydroxylation, dealkylation and alkyl chain oxidation processes (Zhang et al., 2018). And ten intermediates were identified by LC-MS and listed in Table S5. For pathway (I), ROS attack on the Cl4 and N20 sites resulted in the production of P1 ($m/z = 169.1$) and P2 ($m/z = 127.05$) (Lai et al., 2020). For pathway (II) and (III), the dealkylation intermediates like P5 ($m/z = 187.06$), P7 ($m/z = 173.05$) and P6 ($m/z = 145.02$) were generated mainly due to the attack of ROS on the N8 and N20 sites of ATZ (Wei et al., 2022). For pathway (IV), the hydroxylation reaction occurs on the alkyl chain of ATZ to form P8 ($m/z = 231.09$) (Deng et al., 2021). After that, P8 was rapidly transformed into P9 ($m/z = 189.04$) and P10 ($m/z = 211.11$) by dechlorination-hydroxylation reaction, dealkylation and hydroxylation reaction. Subsequently, P6, P9 and P10 were further oxidized to produce P2, P3 ($m/z = 129.02$) and P4 ($m/z = 113.02$). Finally, some of intermediates of ATZ are mineralized to CO_2 and H_2O.

During the degradation of ATZ, it is necessary to analyze the toxicity of the intermediates. The fathead minnow LC50 (96 h), Daphnia magna LC50 (48 h), oral rat LD50, bioaccumulation factor, developmental toxicity and mutagenicity of ATZ and its intermediates were assessed by using Toxicity Estimation Software (T.E.S.T.). The fathead minnow LC50 (96 h) of ATZ was 21.12 mg/L, which was harmful (Fig. 10a). After degradation, the toxicity of the intermediates was reduced compared to ATZ, and some of them were harmless. Fig. 10b showed that the FM-0.96/PMS system can reduce the Daphnia magna LC50 (48 h) of most of the intermediates, and only P3 had higher values. Similarly, ATZ with oral rat LD50 value of 1541.4 mg/L was considered "toxic", and the oral rat LD50 values of most of the intermediates were increased, implying that their toxicity was reduced (Fig. 10c). The FM-0.96/PMS system lowered the bioaccumulation factor and developmental toxicity of most intermediates (Fig. 10d-e). Besides, mutagenicity of ATZ was greatly reduced (Fig. 10f). Meanwhile, the TOC removal degree was evaluated in FM-0.96/PMS/ATZ system. As exhibited in Fig. S11, the TOC removal degree was 40.0% in FM-0.96/PMS/ATZ system within 60.0 min, implying that ATZ could be partly mineralized into CO_2 and H_2O. Based on the above results, the synthesized FM-0.96 not only lowers the toxicity of ATZ but also mineralizes some intermediate products of ATZ into CO_2 and H_2O.

3.7. Reusability and stability of FM-0.96 for ATZ degradation by activating PMS

The reusability and stability of the FM-0.96 were crucial for the long-term treatment of wastewater. As shown in Fig. 11a, the FM-0.96 exhibited satisfactory reusability. In addition, the metal leaching of Fe
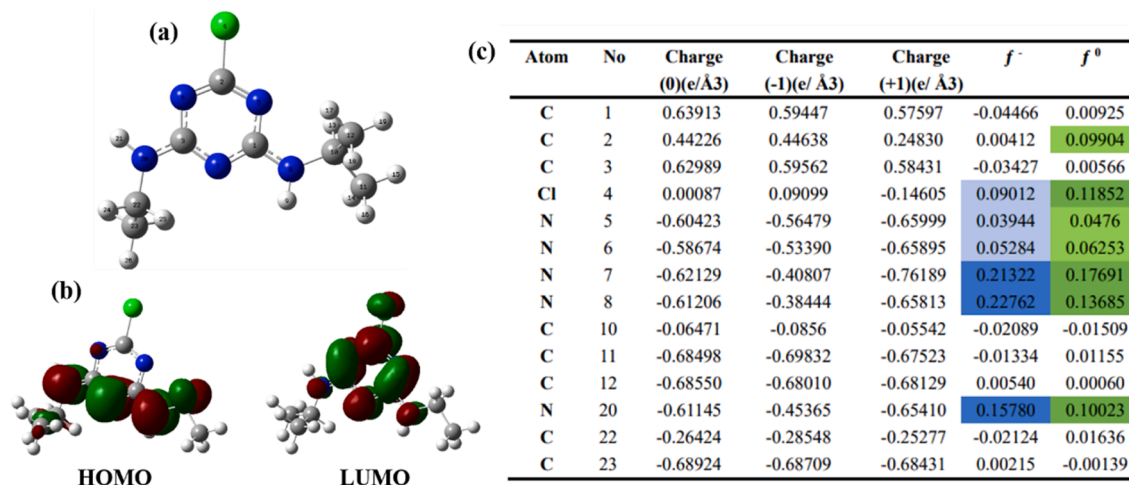

Atom	No	Charge (0)(e/Å3)	Charge (-1)(e/Å3)	Charge (+1)(e/Å3)	f^-	f^0
C	1	0.63913	0.59447	0.57597	-0.04466	0.00925
C	2	0.44226	0.44638	0.24830	0.00412	0.09904
C	3	0.62989	0.59562	0.58431	-0.03427	0.00566
Cl	4	0.00087	0.09099	-0.14605	0.09012	0.11852
N	5	-0.60423	-0.56479	-0.65999	0.03944	0.0476
N	6	-0.58674	-0.53390	-0.65895	0.05284	0.06253
N	7	-0.62129	-0.40807	-0.76189	0.21322	0.17691
N	8	-0.61206	-0.38444	-0.65813	0.22762	0.13685
C	10	-0.06471	-0.0856	-0.05542	-0.02089	-0.01509
C	11	-0.68498	-0.69832	-0.67523	-0.01334	0.01155
C	12	-0.68550	-0.68010	-0.68129	0.00540	0.00060
N	20	-0.61145	-0.45365	-0.65410	0.15780	0.10023
C	22	-0.26424	-0.28548	-0.25277	-0.02124	0.01636
C	23	-0.68924	-0.68709	-0.68431	0.00215	-0.00139

Fig. 8. (a) The chemical structure of ATZ. (b) The HOMO and LUMO orbital of ATZ. (c) The Fukui index of ATZ.
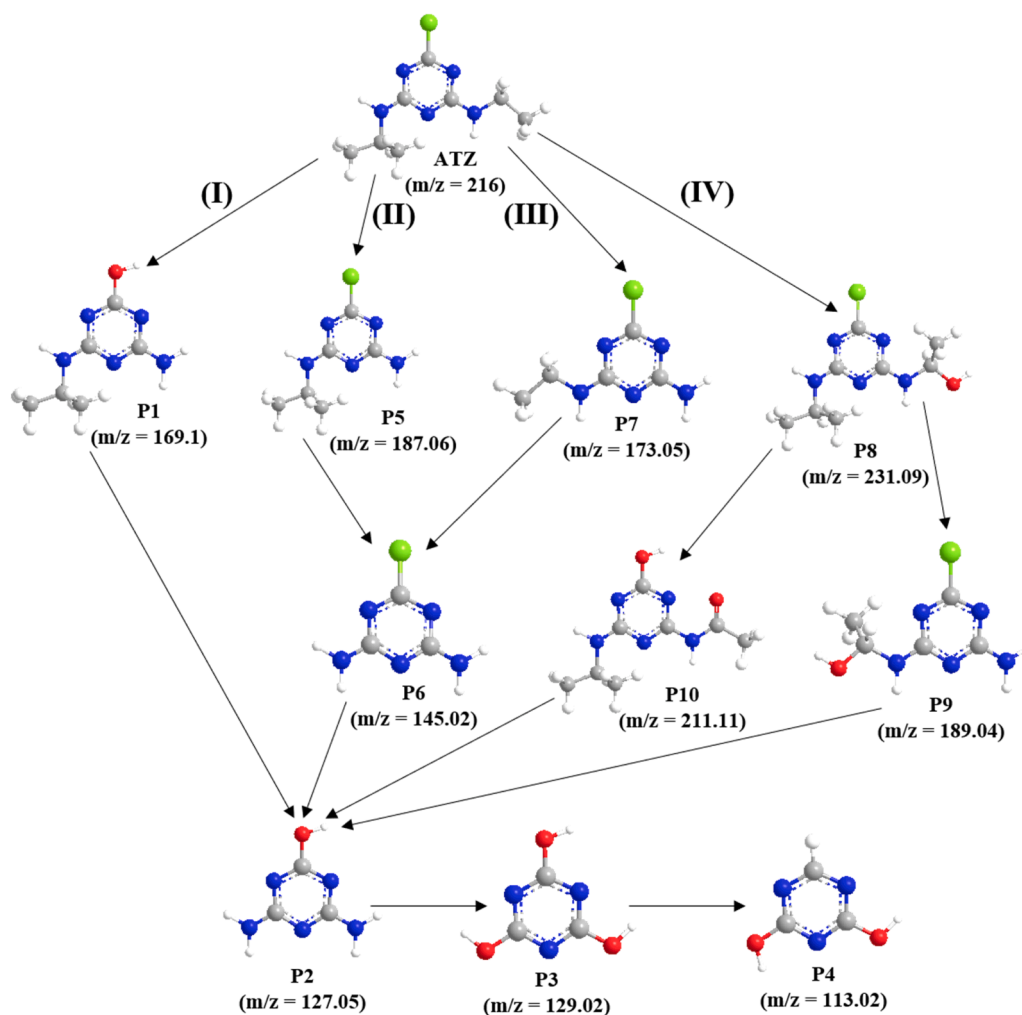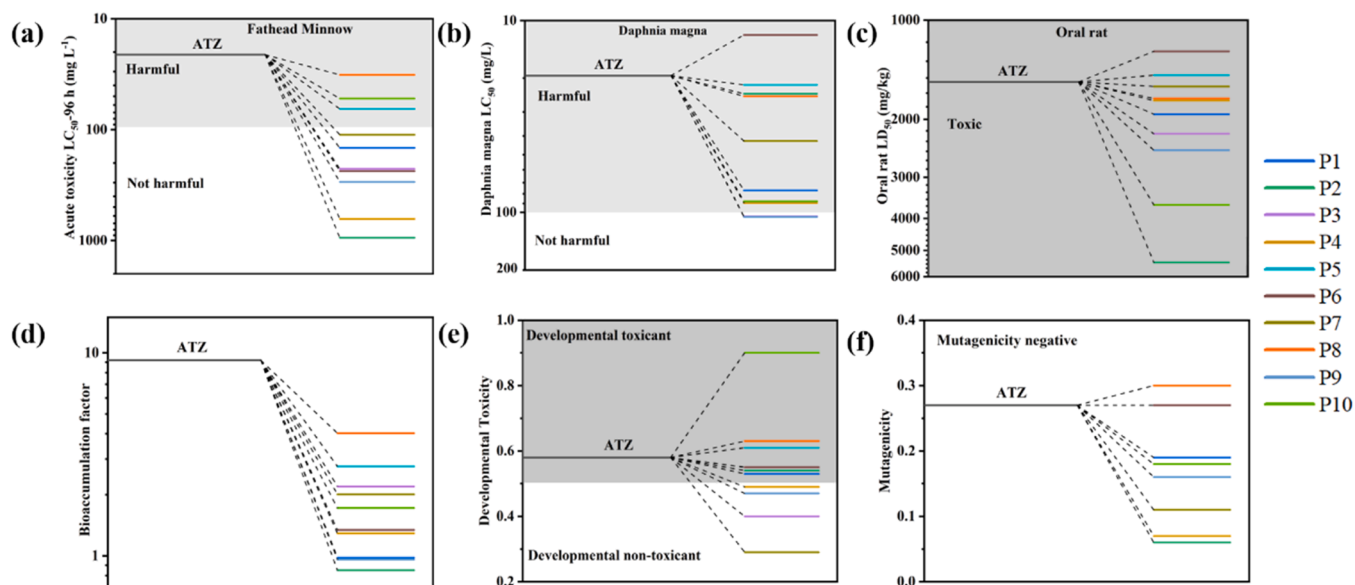
Fig. 9. The possible pathway of ATZ degradation in FM-0.96/PMS system.

Fig. 10. (a) Fathead minnow LC50 (96 h), (b) Daphnia magna LC50 (48 h), (c) Oral rat LD50, (d) Bioaccumulation factor, (e) Developmental toxicity and (f) Mutagenicity of ATZ and its degradation intermediates.
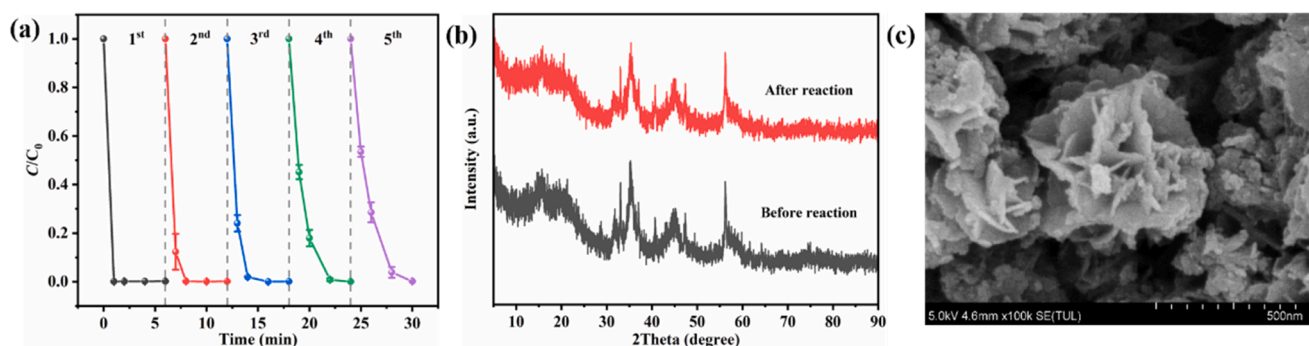
Fig. 11. (a) Reusability, (b) the PXRD patterns and (c) the SEM image of FM-0.96 before and after five cycles. Reaction conditions: ATZ = 10.0 mg/L, PMS = 0.15 mM, Catalyst = 0.2 g/L, initial pH = 5.8, PMS/ATZ molar ratio = 3.25.

and Mo was investigated by ICP-OES after five cycles (Fig. S12), and the concentrations of leached Fe were 2.0, 1.73, 1.51, 1.06 and 0.97 mg/L, respectively, which conformed to the discharge standard of iron ions (Zhang et al., 2021b). Meanwhile, the concentrations of the leached Mo ions were determined as 4.91, 2.60, 2.17, 1.84 and 1.63 mg/L respectively. Compared to other MoS$_2$-activated PMS systems (Lu et al., 2021; Sheng et al., 2019), the concentrations of leached Mo were very low. As shown in Fig. 11b-c, The PXRD pattern as well as SEM image of FM-0.96 did not change obviously after five cycles, which proved the good stability of FM-0.96.

3.8. The continuous operation over FM-0.96 in a fixed membrane reactor

Based on the excellent catalytic performance and cycling stability of FM-0.96, we prepared a fixed membrane reactor for continuous treatment of simulated wastewater by immobilizing FM-0.96 on filter papers (Fig. 12a-b). The degradation performance of the FM-0.96 fixed membrane was evaluated by using 1.0 mg/L and 10.0 mg/L ATZ as simulated

wastewater for continuous operation. By calculation, the hydraulic retention time (HRT) was 5.0 min. As exhibited in Fig. 13a-b, for 10.0 mg/L ATZ, the removal degree of the pure PMS system did not exceed 3.5% for the simulated wastewater, while the removal degree reaches 100.0% within 24.0 h in the FM-0.96 membrane/PMS system. Even after 38.0 h, the removal degree still maintained more than 90.0%. Similarly, for 1.0 mg/L ATZ, the removal degree was not decreased even up to 52.0 h. The percentage of metal ions leached from the catalyst during continuous operation was calculated. For aqueous solution containing 10.0 mg/L ATZ, the percentage of leached Fe and Mo from catalyst was 2.86% and 8.06%, respectively. For the solution containing 1.0 mg/L ATZ, the percentage of leaching Fe and Mo from catalyst was 3.30% and 9.97%, respectively. In addition, the concentrations of leached Mo and Fe ions were 20.0 and 5.0 mg/L, respectively (Fig. S13a-b). In the Fe (5.0 mg/L)-Mo (20.0 mg/L)-PMS homogeneous system, only 10.0% of ATZ was removed (Fig. S13c), indicating the crucial role of the heterogeneous catalysis for FM-0.96. More importantly, it can be calculated that 1.0 Kg FM-0.96 can purify 78.0 t wastewater with an
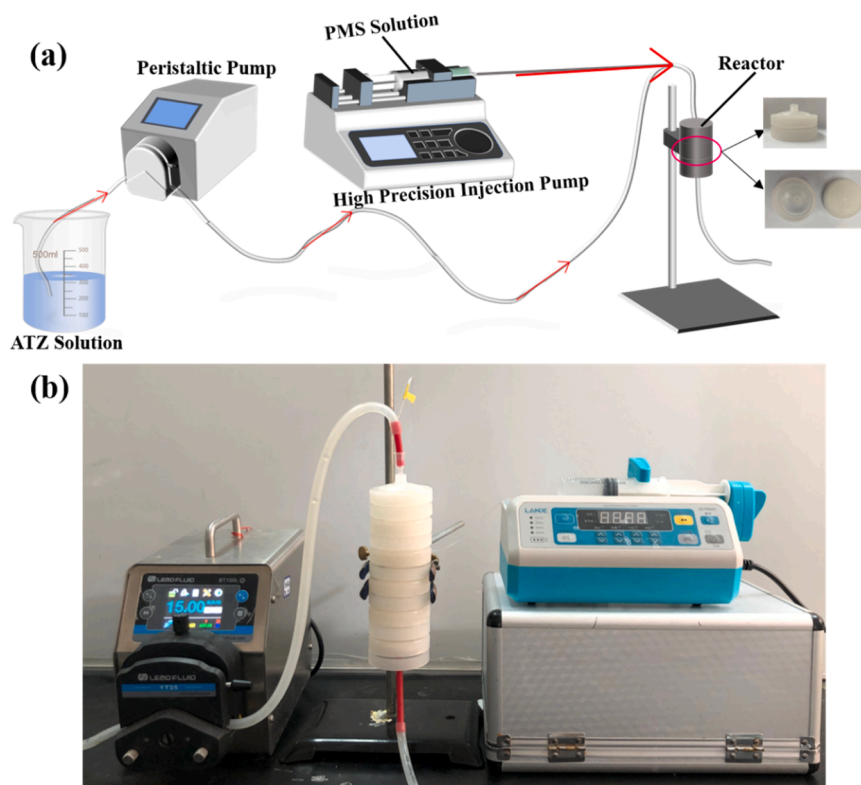

Fig. 12. (a) The schematic illustration and (b) photograph of the fixed membrane reactor.
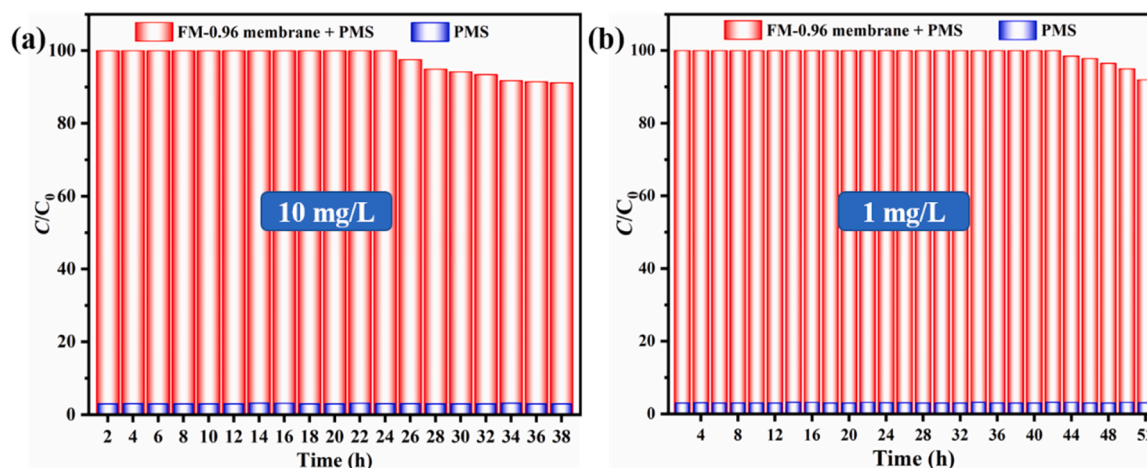
Fig. 13. Continuous operation on ATZ removal degree of FM-0.96 in a fixed membrane reactor (a) 10.0 mg/L; (b) 1.0 mg/L.

initial concentration of 1.0 mg/L ATZ within 52.0 h. In a word, the above results showed that the FM-0.96 membrane has good potential for practical applications.

4. Conclusions

In summary, $FeS_x@MoS_2$-x composites derived from MIL-88A were successfully prepared, and the FM-0.96 exhibited the best catalytic performance on atrazine (ATZ) degradation via peroxymonosulfate (PMS) activation. The rate constant k of FM-0.96 was about 40 and 320 times higher than that of the FeS_x/PMS and MoS_2/PMS, respectively, which could be attributed to the rapid regeneration of Fe^{2+} resulting from the heterogeneous interface. The free radical ($SO_4\cdot^-$ and $\cdot OH$) and non-free radical ($^1O_2$) played the primary role in the FM-0.96/PMS/ATZ system. Furthermore, the total organic carbon was removed by about 40.0% within 60.0 min, and the toxicities of ATZ and most of its intermediates were greatly reduced. In addition, continuous treatment of wastewater was realized using a self-developed fixed membrane reactor, and 1.0 Kg FM-0.96 can achieve an effective purification of 78.0 t wastewater with an initial concentration of 1.0 mg/L ATZ within 52.0 h without obvious decline of removal degree. This work provides an intensive insight into PMS activation in environment remediation by transition-metal sulfides composites derived from metal-organic frameworks.

Environmental implication

Atrazine (ATZ) was considered be detrimental to the environment and public health due to its long persistence and low biodegradability properties. In this work, $FeS_x@MoS_2$-x (FM-x, x implied real Mo/Fe content ratios) catalyst was synthesized adopting MIL-88A as precursor to degrade ATZ by activating peroxymonosulfate (PMS). ATZ could be completely degraded within 1.0 min over FM-0.96, in which the toxicities for most of its intermediates were greatly reduced. This work provides an approach for PMS activation in environment remediation by transition-metal sulfides composites derived from metal-organic frameworks.

CRediT authorship contribution statement

Fei Wang: Data curation, Investigation, Visualization, Software, Writing – original draft. **Shan-Shan Liu:** Data curation, Methodology. **Ziyue Feng:** Software, Methodology. **Huifen Fu:** Conceptualization, Funding acquisition, Supervision, Project administration, Writing – review & editing. **Mengyu Wang:** Software, Methodology. **Peng Wang:** Resources. **Wen Liu:** Validation. **Chong-Chen Wang:**

Conceptualization, Funding acquisition, Supervision, Project administration, Writing – review & editing.

Declaration of Competing Interest

The authors declare that they have no known competing financial interests or personal relationships that could have appeared to influence the work reported in this paper.

Data Availability

Data will be made available on request.

Appendix A. Supporting information

Supplementary data associated with this article can be found in the online version at doi:10.1016/j.jhazmat.2022.129723.

References

Chen, L., Ji, H., Qi, J., Huang, T., Wang, C.-C., Liu, W., 2021a. Degradation of acetaminophen by activated peroxymonosulfate using Co(OH)₂ hollow microsphere supported titanate nanotubes: insights into sulfate radical production pathway through CoOH⁺ activation. Chem. Eng. J. 406, 126877 https://doi.org/10.1016/j.cej.2020.126877.

Chen, Y., Lan, S., Zhu, M., 2021b. Construction of piezoelectric BaTiO₃/MoS₂ heterojunction for boosting piezo-activation of peroxymonosulfate. Chin. Chem. Lett. 32 (6), 2052–2056. https://doi.org/10.1016/j.cclet.2020.11.016.

Chen, Z., Lian, C., Huang, K., Ji, J., Yan, Q., Zhang, J., Xing, M., 2022. "Small amount for multiple times" of H₂O₂ feeding way in MoS₂-Feₓ heterogeneous fenton for enhancing sulfadiazine degradation. Chin. Chem. Lett. 33 (3), 1365–1372. https://doi.org/10.1016/j.cclet.2021.08.016.

Deng, S., Liu, L., Cagnetta, G., Huang, J., Yu, G., 2021. Mechanochemically synthesized S-ZVIbm composites for the activation of persulfate in the pH-independent degradation of atrazine: effects of sulfur dose and ball-milling conditions. Chem. Eng. J. 423, 129789 https://doi.org/10.1016/j.cej.2021.129789.

Dong, X., Ren, B., Zhang, X., Liu, X., Sun, Z., Li, C., Tan, Y., Yang, S., Zheng, S., Dionysiou, D.D., 2020. Diatomite supported hierarchical 2D CoNi₃O₄ nanoribbons as highly efficient peroxymonosulfate catalyst for atrazine degradation. Appl. Catal. B: Environ. 272, 118971 https://doi.org/10.1016/j.apcatb.2020.118971.

Du, A., Fu, H., Wang, P., Zhao, C., Wang, C.-C., 2022a. Enhanced catalytic peroxymonosulfate activation for sulfonamide antibiotics degradation over the

supported CoS$_x$-CuS$_x$ derived from ZIF-L(Co) immobilized on copper foam. J. Hazard. Mater. 426, 128134 https://doi.org/10.1016/j.jhazmat.2021.128134.

Du, M., Yi, Q., Ji, J., Zhu, Q., Duan, H., Xing, M., Zhang, J., 2020. Sustainable activation of peroxymonosulfate by the Mo(IV) in MoS$_2$ for the remediation of aromatic organic pollutants. Chin. Chem. Lett. 31 (10), 2803–2808. https://doi.org/10.1016/j.cclet.2020.08.002.

Du, X., Wang, S., Ye, F., Qingrui, Z., 2022b. Derivatives of metal-organic frameworks for heterogeneous Fenton-like processes: From preparation to performance and mechanisms in wastewater purification – a mini review. Environ. Res. 206, 112414 https://doi.org/10.1016/j.envres.2021.112414.

Duan, X., Li, W., Ao, Z., Kang, J., Tian, W., Zhang, H., Ho, S.-H., Sun, H., Wang, S., 2019. Origins of boron catalysis in peroxymonosulfate activation and advanced oxidation. J. Mater. Chem. A 7 (41), 23904–23913. https://doi.org/10.1039/C9TA04885E.

Fan, Y., Ji, Y., Zheng, G., Lu, J., Kong, D., Yin, X., Zhou, Q., 2017. Degradation of atrazine in heterogeneous Co$_3$O$_4$ activated peroxymonosulfate oxidation process: Kinetics, mechanisms, and reaction pathways. Chem. Eng. J. 330, 831–839. https://doi.org/10.1016/j.cej.2017.08.020.

Fu, H., Wang, C.-C., Liu, W., 2021. MOFs for water purification. Chin. Chem. Lett. https://doi.org/10.1016/j.cclet.2021.08.065.

Geng, P., Yu, N., Macharia, D.K., Meng, R., Qiu, P., Tao, C., Li, M., Zhang, H., Chen, Z., Lian, W., 2022. MOF-derived CuS@Cu-MOF nanocomposites for synergistic photothermal-chemodynamic-chemo therapy. Chem. Eng. J. 441, 135964 https://doi.org/10.1016/j.cej.2022.135964.

Hang, J., Yi, X.-H., Wang, C.-C., Fu, H., Wang, P., Zhao, Y., 2022. Heterogeneous photo-Fenton degradation toward sulfonamide matrix over magnetic Fe$_3$S$_4$ derived from MIL-100(Fe). J. Hazard. Mater. 424, 127415 https://doi.org/10.1016/j.jhazmat.2021.127415.

He, S., Chen, Y., Li, X., Zeng, L., Zhu, M., 2022. Heterogeneous photocatalytic activation of persulfate for the removal of organic contaminants in water: a critical review. ACS EST Eng. 2 (4), 527–546. https://doi.org/10.1021/acsestengg.1c00330.

Hu, J., Chen, H., Dong, H., Zhu, L., Qiang, Z., Yu, J., 2021. Transformation of iopamidol and atrazine by peroxymonosulfate under catalysis of a composite iron corrosion product (Fe/Fe$_3$O$_4$): electron transfer, active species and reaction pathways. J. Hazard. Mater. 403, 123553 https://doi.org/10.1016/j.jhazmat.2020.123553.

Huo, Z., Xia, L., Li, G., Xiao, X., 2020. A "polymer template" strategy for carbonized polymer dots with controllable properties. Chem. Eur. J. 26 (64), 14754–14764. https://doi.org/10.1002/chem.202003379.

Ji, F., Zhang, H., Wei, X., Zhang, Y., Lai, B., 2019. Efficient degradation of atrazine by Co-NZ catalyst prepared by electroless plating in the presence of peroxymonosulfate: characterization, performance and mechanistic consideration. Chem. Eng. J. 359, 1316–1326. https://doi.org/10.1016/j.cej.2018.11.049.

Lai, L., Zhou, H., Zhang, H., Ao, Z., Pan, Z., Chen, Q., Xiong, Z., Yao, G., Lai, B., 2020. Activation of peroxydisulfate by natural titanomagnetite for atrazine removal via free radicals and high-valent iron-oxo species. Chem. Eng. J. 387, 124165 https://doi.org/10.1016/j.cej.2020.124165.

Lan, S., Jing, B., Yu, C., Yan, D., Li, Z., Ao, Z., Zhu, M., 2022. Protrudent iron single-atom accelerated interfacial piezoelectric polarization for self-powered water motion triggered fenton-like reaction. Small 18 (2), 2105279. https://doi.org/10.1002/smll.202105279.

Li, C., Wu, J., Peng, W., Fang, Z., Liu, J., 2019a. Peroxymonosulfate activation for efficient sulfamethoxazole degradation by Fe$_3$O$_4$/β-FeOOH nanocomposites: coexistence of radical and non-radical reactions. Chem. Eng. J. 356, 904–914. https://doi.org/10.1016/j.cej.2018.09.064.

Li, D., Li, H., Long, M., Bai, X., Zhao, Q., Wen, Q., Song, F., 2022a. Synergetic effect of photocatalysis and peroxymonosulfate activation by MIL-53Fe@TiO$_2$ on efficient degradation of tetracycline hydrochloride under visible light irradiation. CrystEngComm 24 (23), 4283–4293. https://doi.org/10.1039/D2CE00372D.

Li, H., Shan, C., Li, W., Pan, B., 2018a. Peroxymonosulfate activation by iron(III)-tetraamidomacrocyclic ligand for degradation of organic pollutants via high-valent iron-oxo complex. Water Res. 147, 233–241. https://doi.org/10.1016/j.watres.2018.10.015.

Li, J., Xu, M., Yao, G., Lai, B., 2018b. Enhancement of the degradation of atrazine through CoFe$_2$O$_4$ activated peroxymonosulfate (PMS) process: kinetic, degradation intermediates, and toxicity evaluation. Chem. Eng. J. 348, 1012–1024. https://doi.org/10.1016/j.cej.2018.05.032.

Li, J., Wan, Y., Li, Y., Yao, G., Lai, B., 2019b. Surface Fe(III)/Fe(II) cycle promoted the degradation of atrazine by peroxymonosulfate activation in the presence of hydroxylamine. Appl. Catal. B: Environ. 256, 117782 https://doi.org/10.1016/j.apcatb.2019.117782.

Li, J., Gou, G., Zhao, H., Liu, C., Li, N., Li, L., Tan, B., Lai, B., 2022b. Efficient peroxymonosulfate activation by CoFe$_2$O$_4$-CeO$_2$ composite: performance and catalytic mechanism. Chem. Eng. J. 435, 134840 https://doi.org/10.1016/j.cej.2022.134840.

Li, X., Liao, F., Ye, L., Yeh, L., 2020. Controlled pyrolysis of MIL-88A to prepare iron/carbon composites for synergistic persulfate oxidation of phenol: catalytic performance and mechanism. J. Hazard. Mater. 398, 122938 https://doi.org/10.1016/j.jhazmat.2020.122938.

Li, X., Liu, X., Huang, X., Lin, C., He, M., Ouyang, W., 2021a. Activation of peroxymonosulfate by WTRs-based iron-carbon composites for atrazine removal: Performance evaluation, mechanism insight and byproduct analysis. Chem. Eng. J. 421, 127811 https://doi.org/10.1016/j.cej.2021.127811.

Li, Y., Wang, C.-C., Zeng, X., Sun, X.-Z., Zhao, C., Fu, H., Wang, P., 2022c. Seignette salt induced defects in Zr-MOFs for boosted Pb(II) adsorption: universal strategy and mechanism insight. Chem. Eng. J. 442, 136276 https://doi.org/10.1016/j.cej.2022.136276.

Li, Y., Dong, H., Li, L., Tang, L., Tian, R., Li, R., Chen, J., Xie, Q., Jin, Z., Xiao, J., 2021b. Recent advances in wastewater treatment through transition metal sulfides-based advanced oxidation processes. Water Res., 116850 https://doi.org/10.1016/j.watres.2021.116850.

Liu, B., Guo, W., Wang, H., Si, Q., Zhao, Q., Luo, H., Ren, N., 2020. Activation of peroxymonosulfate by cobalt-impregnated biochar for atrazine degradation: the pivotal roles of persistent free radicals and ecotoxicity assessment. J. Hazard. Mater. 398, 122768 https://doi.org/10.1016/j.jhazmat.2020.122768.

Lu, H., Shi, H., Xie, Q., Li, L., Xiao, Y., Jia, L., Li, D., 2022. Surface modification of Co$_3$O$_4$ nanosheets to promote peroxymonosulfate activation for degradation of atrazine. Catal. Lett. https://doi.org/10.1007/s10562-021-03874-4.

Lu, J., Zhou, Y., Zhou, Y., 2021. Efficiently activate peroxymonosulfate by Fe$_3$O$_4$@MoS$_2$ for rapid degradation of sulfonamides. Chem. Eng. J. 422, 130126 https://doi.org/10.1016/j.cej.2021.130126.

Luo, X., Bai, L., Xing, J., Zhu, X., Xu, D., Xie, B., Gan, Z., Li, G., Liang, H., 2019. Ordered mesoporous cobalt Containing perovskite as a high-performance heterogeneous catalyst in activation of peroxymonosulfate. ACS Appl. Mater. Interfaces 11 (39), 35720–35728. https://doi.org/10.1021/acsami.9b11322.

Nie, G., Xiao, L., Bi, J., Wang, S., Duan, X., 2022. New insight to piezocatalytic peroxymonosulfate activation: the critical role of dissolved oxygen in mediating radical and nonradical pathways. Appl. Catal. B: Environ. 315, 121584 https://doi.org/10.1016/j.apcatb.2022.121584.

Peng, L., Shang, Y., Gao, B., Xu, X., 2021. Co$_3$O$_4$ anchored in N, S heteroatom co-doped porous carbons for degradation of organic contaminant: role of pyridinic N-Co binding and high tolerance of chloride. Appl. Catal. B: Environ. 282, 119484 https://doi.org/10.1016/j.apcatb.2020.119484.

Peng, X., Yang, Z., Hu, F., Tan, C., Pan, Q., Dai, H., 2022. Mechanistic investigation of rapid catalytic degradation of tetracycline using CoFe$_2$O$_4$@MoS$_2$ by activation of peroxymonosulfate. Sep. Purif. Technol. 287, 120525 https://doi.org/10.1016/j.seppur.2022.120525.

Ren, X., Wang, C.-C., Li, Y., Wang, C.-Y., Wang, P., Gao, S., 2022. Ag(I) removal and recovery from wastewater adopting NH$_2$-MIL-125 as efficient adsorbent: a 3Rs (reduce, recycle and reuse) approach and practice. Chem. Eng. J. 442, 136306 https://doi.org/10.1016/j.cej.2022.136306.

Roy, D., Neogi, S., De, S., 2022. Visible light assisted activation of peroxymonosulfate by bimetallic MOF based heterojunction MIL-53(Fe/Co)/CeO$_2$ for atrazine degradation: pivotal roles of dual redox cycle for reactive species generation. Chem. Eng. J. 430, 133069 https://doi.org/10.1016/j.cej.2021.133069.

Shen, Z., Zhou, H., Pan, Z., Guo, Y., Yuan, Y., Yao, G., Lai, B., 2020. Degradation of atrazine by Bi$_2$MoO$_6$ activated peroxymonosulfate under visible light irradiation. J. Hazard. Mater. 400, 123187 https://doi.org/10.1016/j.jhazmat.2020.123187.

Sheng, B., Yang, F., Wang, Y., Wang, Z., Li, Q., Guo, Y., Lou, X., Liu, J., 2019. Pivotal roles of MoS$_2$ in boosting catalytic degradation of aqueous organic pollutants by Fe (II)/PMS. Chem. Eng. J. 375, 121989 https://doi.org/10.1016/j.cej.2019.121989.

Sun, Y., Li, R., Song, C., Zhang, H., Cheng, Y., Nie, A., Li, H., Dionysiou, D.D., Qian, J., Pan, B., 2021a. Origin of the improved reactivity of MoS$_2$ single crystal by confining lattice Fe atom in peroxymonosulfate-based Fenton-like reaction. Appl. Catal. B: Environ. 298, 120537 https://doi.org/10.1016/j.apcatb.2021.120537.

Sun, Z., Liu, X., Dong, X., Zhang, X., Tan, Y., Yuan, F., Zheng, S., Li, C., 2021b. Synergistic activation of peroxymonosulfate via in situ growth FeCo$_2$O$_4$ nanoparticles on natural rectorite: role of transition metal ions and hydroxyl groups. Chemosphere 263, 127965. https://doi.org/10.1016/j.chemosphere.2020.127965.

Tang, R., Gong, D., Deng, Y., Xiong, S., Deng, J., Li, L., Zhou, Z., Zheng, J., Su, L., Yang, L., 2022. π-π Stacked step-scheme PDI/g-C$_3$N$_4$/TiO$_2$@Ti$_3$C$_2$ photocatalyst with enhanced visible photocatalytic degradation towards atrazine via peroxymonosulfate activation. Chem. Eng. J. 427, 131809 https://doi.org/10.1016/j.cej.2021.131809.

Wang, C., Ma, L., Wang, C.-C., Wang, P., Gutierrez, L., Zheng, W., 2022a. Light-response adsorption and desorption behaviors of metal–organic frameworks. Environ. Funct. Mater. https://doi.org/10.1016/j.efmat.2022.05.002.

Wang, C., Wang, C.-C., Zhang, X.-W., Ren, X.-Y., Yu, B., Wang, P., Zhao, Z.-X., Fu, H., 2021. A new Eu-MOF for ratiometrically fluorescent detection toward quinolone antibiotics and selective detection toward tetracycline antibiotics. Chin. Chem. Lett. https://doi.org/10.1016/j.cclet.2021.08.095.

Wang, F., Fu, H., Wang, F.-X., Zhang, X.-W., Wang, P., Zhao, C., Wang, C.-C., 2022b. Enhanced catalytic sulfamethoxazole degradation via peroxymonosulfate activation over amorphous CoS$_x$@SiO$_2$ nanocages derived from ZIF-67. J. Hazard. Mater. 423, 126998 https://doi.org/10.1016/j.jhazmat.2021.126998.

Wang, F.X., Wang, C.-C., Du, X., Li, Y., Wang, F., Wang, P., 2022c. Efficient removal of emerging organic contaminants via photo-Fenton process over micron-sized Fe-MOF sheet. Chem. Eng. J. 429, 132495 https://doi.org/10.1016/j.cej.2021.132495.

Wang, J., Yi, X.-H., Xu, X., Ji, H., Alanazi, A.M., Wang, C.-C., Zhao, C., Kaneti, Y.V., Wang, P., Liu, X., Yamauchi, Y., 2022d. Eliminating tetracycline antibiotics matrix via photoactivated sulfate radical-based advanced oxidation process over the immobilized MIL-88A: Batch and continuous experiments. Chem. Eng. J. 431, 133213 https://doi.org/10.1016/j.cej.2021.133213.

Wang, P., Liu, X., Qiu, W., Wang, F., Jiang, H., Chen, M., Zhang, W., Ma, J., 2020. Catalytic degradation of micropollutant by peroxymonosulfate activation through Fe (III)/Fe(II) cycle confined in the nanoscale interlayer of Fe(III)-saturated montmorillonite. Water Res. 182, 116030 https://doi.org/10.1016/j.watres.2020.116030.

Wei, K., Armutlulu, A., Wang, Y., Yao, G., Xie, R., Lai, B., 2022. Visible-light-driven removal of atrazine by durable hollow core-shell TiO$_2$@LaFeO$_3$ heterojunction coupling with peroxymonosulfate via enhanced electron-transfer. Appl. Catal. B: Environ. 303, 120889 https://doi.org/10.1016/j.apcatb.2021.120889.

Wu, H., Chen, X., Zhang, X., Jiang, Z., Dong, Y., Li, H., Ni, L., Diao, G., Chen, M., 2022. Multidimensional nanobox structural carbon nanofibers with dual confined effect for boosting storage performance and electrochemical kinetics of alkali metal ion batteries. Chem. Eng. J. 428, 131207 https://doi.org/10.1016/j.cej.2021.131207.

Wu, L., Wang, C.-C., Chu, H.-Y., Yi, X.-H., Wang, P., Zhao, C., Fu, H., 2021. Bisphenol A cleanup over MIL-100(Fe)/CoS composites: pivotal role of Fe–S bond in regenerating Fe^{2+} ions for boosted degradation performance. Chemosphere 280, 130659. https://doi.org/10.1016/j.chemosphere.2021.130659.

Wu, S., He, H., Li, X., Yang, C., Zeng, G., Wu, B., He, S., Lu, L., 2018. Insights into atrazine degradation by persulfate activation using composite of nanoscale zero-valent iron and graphene: performances and mechanisms. Chem. Eng. J. 341, 126–136. https://doi.org/10.1016/j.cej.2018.01.136.

Xu, H., Sheng, Y., 2021. New insights into the degradation of chloramphenicol and fluoroquinolone antibiotics by peroxymonosulfate activated with FeS: Performance and mechanism. Chem. Eng. J. 414, 128823 https://doi.org/10.1016/j.cej.2021.128823.

Yang, Y., Banerjee, G., Brudvig, G.W., Kim, J.-H., Pignatello, J.J., 2018. Oxidation of Organic Compounds in Water by Unactivated Peroxymonosulfate. Environ. Sci. Technol. 52 (10), 5911–5919. https://doi.org/10.1021/acs.est.8b00735.

Yang, Y., Zhang, P., Hu, K., Zhou, P., Wang, Y., Asif, A.H., Duan, X., Sun, H., Wang, S., 2022. Crystallinity and valence states of manganese oxides in Fenton-like polymerization of phenolic pollutants for carbon recycling against degradation. Appl. Catal. B: Environ. 315, 121593 https://doi.org/10.1016/j.apcatb.2022.121593.

Yi, X.-H., Ji, H., Wang, C.-C., Li, Y., Li, Y.-H., Zhao, C., Wang, A., Fu, H., Wang, P., Zhao, X., 2021. Photocatalysis-activated SR-AOP over PDINH/MIL-88A (Fe) composites for boosted chloroquine phosphate degradation: performance, mechanism, pathway and DFT calculations. Appl. Catal. B: Environ. 293, 120229 https://doi.org/10.1016/j.apcatb.2021.120229.

Yu, C., He, J., Lan, S., Guo, W., Zhu, M., 2022. Enhanced utilization efficiency of peroxymonosulfate via water vortex-driven piezo-activation for removing organic contaminants from water. Environ. Sci. Ecotechnol. 10, 100165 https://doi.org/10.1016/j.ese.2022.100165.

Yun, E.-T., Lee, J.H., Kim, J., Park, H.-D., Lee, J., 2018. Identifying the nonradical mechanism in the peroxymonosulfate activation process: singlet oxygenation versus mediated electron transfer. Environ. Sci. Technol. 52 (12), 7032–7042. https://doi.org/10.1021/acs.est.8b00959.

Zeng, Z., Khan, A., Wang, Z., Zhao, M., Mo, W., Chen, Z., 2020. Elimination of atrazine through radical/non-radical combined processes by manganese nano-catalysts/PMS and implications to the structure-performance relationship. Chem. Eng. J. 397, 125425 https://doi.org/10.1016/j.cej.2020.125425.

Zhang, H., Liu, X., Ma, J., Lin, C., Qi, C., Li, X., Zhou, Z., Fan, G., 2018. Activation of peroxymonosulfate using drinking water treatment residuals for the degradation of atrazine. J. Hazard. Mater. 344, 1220–1228. https://doi.org/10.1016/j.jhazmat.2017.11.038.

Zhang, L.-S., Jiang, X.-H., Zhong, Z.-A., Tian, L., Sun, Q., Cui, Y.-T., Lu, X., Zou, J.-P., Luo, S.-L., 2021a. Carbon Nitride Supported High-Loading Fe Single-Atom Catalyst for Activation of Peroxymonosulfate to Generate $^{1}O_2$ with 100 % Selectivity. Angew. Chem. Int. Ed. 60 (40), 21751–21755. https://doi.org/10.1002/anie.202109488.

Zhang, X., Wang, F., Wang, C.-C., Wang, P., Fu, H., Zhao, C., 2021b. Photocatalysis activation of peroxodisulfate over the supported Fe_3O_4 catalyst derived from MIL-88A (Fe) for efficient tetracycline hydrochloride degradation. Chem. Eng. J. 426, 131927 https://doi.org/10.1016/j.cej.2021.131927.

Zhang, X.-W., Lan, M.-Y., Wang, F., Yi, X.-H., Wang, C.-C., 2022. ZIF-67-based catalysts in persulfate advanced oxidation processes (PS-AOPs) for water remediation. J. Environ. Chem. Eng. 10 (3), 107997 https://doi.org/10.1016/j.jece.2022.107997.

Zhao, J., Li, F., Wei, H., Ai, H., Gu, L., Chen, J., Zhang, L., Chi, M., Zhai, J., 2021. Superior performance of ZnCoOx/peroxymonosulfate system for organic pollutants removal by enhancing singlet oxygen generation: the effect of oxygen vacancies. Chem. Eng. J. 409, 128150 https://doi.org/10.1016/j.cej.2020.128150.

Zhao, Q., Wang, C.-C., Wang, P., 2022a. Effective norfloxacin elimination via photo-Fenton process over the MIL-101(Fe)-NH_2 immobilized on α-Al_2O_3 sheet. Chin. Chem. Lett. https://doi.org/10.1016/j.cclet.2022.01.033.

Zhao, Q., Yi, X.-H., Wang, C.-C., Wang, P., Zheng, W., 2022b. Photocatalytic Cr (VI) reduction over MIL-101 (Fe)–NH_2 immobilized on alumina substrate: From batch test to continuous operation. Chem. Eng. J. 429, 132497 https://doi.org/10.1016/j.cej.2021.132497.

Zheng, H., Bao, J., Huang, Y., Xiang, L., Ren, B., Du, J., Nadagouda, M.N., Dionysiou, D. D., 2019. Efficient degradation of atrazine with porous sulfurized Fe_2O_3 as catalyst for peroxymonosulfate activation. Appl. Catal. B: Environ. 259, 118056 https://doi.org/10.1016/j.apcatb.2019.118056.